

MSc Geowissenschaften  
Mathematisch-Naturwissenschaftliche Fakultät  
Fachbereich Geowissenschaften  
Eberhard Karls Universität Tübingen

## MASTER THESIS

# MODELLING OF ICE-SHELF CHANNELS: THE INFLUENCE OF CHANNEL WIDTHS ON ICE SHELF STABILITY

*submitted by*  
**Julius Loos**

**Supervision:**  
Jnr. Prof. Dr. Reinhard Drews  
Clemens Schannwell, PhD  
Prof. Dr. Todd Ehlers

September 26, 2019



I hereby declare that this thesis is entirely the result of my own original work. All used sources of information and resources of data are indicated as such and properly acknowledged. I further declare that this or similar work has not been submitted for credit elsewhere.

---

*Place, Date*

---

*Signature*

## **Acknowledgments**

I would like to thank the head of the ESD research group Prof. Todd A. Ehlers for giving me the opportunity to write my master thesis in this diverse group with a broad range of very interesting topics. I would also like to thank my main supervisors Jnr. Prof. Reinhard Drews and Dr. Clemens Schannwell for an excellent supervision during my work. Both were always available for any type of questions. Nevertheless, I had the opportunity to work independently. I would like to thank Johannes Aschauer for proof-reading and his great co-working attitude. Furthermore, I would like to thank my father, Paul Deißinger and Clemens Schannwell for proof-reading parts of my thesis. Thank you Jo, Joni, Paul and the sept-tête for a great company during my studies. Lastly, I want to thank my parents for supporting me during my studies.

## **Abstract**

Longitudinal and curvilinear depressions at the top and the bottom of ice shelves, also known as ice-shelf channels, can alter the stress distribution, thin the ice in their vicinity and hence bias the stability of ice sheet/shelf systems in the Antarctic. These processes may intensify the total ice-sheet mass loss in the polar regions. The origin of such ice-shelf channels is an ongoing subject of research. They may be partly attributed to sedimentary processes near the grounding line, which represents the transition between the grounded ice-sheet and the floating ice-shelf. In this study, the finite element, full-Stokes, ice-sheet/flow model Elmer/Ice is used. A synthetic ice-sheet/shelf model in two and three dimensions is set up. The 2-D model set-up addresses multiple, instantaneous sub-shelf channel widths, shaped by Gaussian-bell functions, whereas the 3- D model initiates channel advection at the grounding line with an uplifted bedrock geometry. The 2-D model results indicate decreasing horizontal shear stress (bridging) with increasing channel width. In addition, a relationship between the deviation of hydrostatic equilibrium and bridging is numerically derived. Furthermore, a non-linear relationship between channel width and the deviation of hydrostatic equilibrium is found. The 3-D model results are qualitatively consistent with 2-D results. However, bridging patterns towards the shelf front can alter and decrease. These findings implicate, that the precise characterization of basal geometries of ice-shelf channels is non-negligible and may draw a new link between imbalances of ice sheet/shelf systems and ice-shelf channel evolution including decay, growth and retention.

# Contents

<b>1. Introduction</b>	<b>1</b>
1.1. Objectives . . . . .	3
<b>2. Theory</b>	<b>4</b>
2.1. Governing equations . . . . .	4
2.2. Hydrostatic equilibrium and horizontal shear stress . . . . .	5
<b>3. Methods</b>	<b>6</b>
3.1. Model description . . . . .	7
3.1.1. Synthetic 2-D ice-shelf set-up . . . . .	9
3.1.2. Synthetic 3-D coupled ice-sheet/shelf set-up . . . . .	10
3.2. Data processing . . . . .	12
<b>4. Results</b>	<b>13</b>
4.1. Deviation of hydrostatic equilibrium (HD) . . . . .	13
4.1.1. Flow velocities . . . . .	14
4.1.2. Horizontal shear stress . . . . .	16
4.1.3. Abutment and channel peak deviation . . . . .	18
4.1.4. Correlation of channel width with deviation of hydrostatic equilibrium . . . . .	19
4.1.5. Influence of the domain size on channel closing . . . . .	20
4.2. Grounding-line sourced ice-shelf channel (3-D) . . . . .	21
<b>5. Discussion</b>	<b>24</b>
5.1. Interpretation of vertical/horizontal velocities and hydrostatic imbalances (2-D) . . . . .	24
5.2. Implications of hydrostatic imbalances on horizontal shear stress . . . . .	25
5.3. Increasing channel width vs. hydrostatic imbalances (2-D and 3-D) . . . . .	26
5.4. Larger shelf domains amplify channel closing (2-D) . . . . .	28
5.5. Induced sub-shelf channel advection with bedrock perturbations (3-D) . . . . .	28
5.6. Remarks and model limitations . . . . .	29
<b>6. Conclusion</b>	<b>31</b>
<b>Bibliography</b>	<b>32</b>
<b>Appendices</b>	<b>36</b>
<b>A. Code and data availability</b>	<b>37</b>
<b>B. Additional equations</b>	<b>38</b>
<b>C. Additional figures and tables</b>	<b>39</b>

## List of Figures

1.	Ice-shelf channels of the Roi Baudouin Ice-Shelf . . . . .	2
2.	Workflow . . . . .	6
3.	Overview of parameters and boundary conditions for 2-D and 3-D model set-up . . . . .	8
4.	Channel widths for 2-D simulation case . . . . .	10
5.	Introduction of deviation of hydrostatic equilibrium with prominent features . . . . .	13
6.	Horizontal ice flow velocities of ice shelf ( $u_x$ ) . . . . .	14
7.	Vertical ice flow velocities of ice shelf ( $u_y$ ) . . . . .	15
8.	Ice flow velocities: cross sections . . . . .	15
9.	Horizontal shear stress ( $\sigma_{xy}$ ) . . . . .	16
10.	Cross-sectional profile of horizontal shear stress and derivative . . . . .	17
11.	Channel peak and abutment deviation . . . . .	18
12.	Root mean square with channel peak deviation vs. channel widths . . . . .	20
13.	Channel closing as a function of domain size . . . . .	21
14.	Channel initialisation with bedrock bump (3-D) . . . . .	22
15.	RMS of hydrostatic deviation (3-D) . . . . .	23
16.	Deformation pattern . . . . .	26
18.	Top and bottom of ice-shelf (all widths) . . . . .	41
19.	All derivatives of top surface and bridging-profiles . . . . .	42

## **List of Tables**

1.	Physical parameters and constants . . . . .	7
2.	2-D model set-up . . . . .	10
3.	3-D model set-up . . . . .	11
4.	Complete summary of 2-D model set-up geometries . . . . .	39

## Abbreviations

### Acronyms

<b>CDW</b>	Circumpolar Deep Water
<b>CW</b>	channel width
<b>CWH</b>	channel half width
<b>FS</b>	full-Stokes
<b>GUI</b>	graphical user interface
<b>HD</b>	deviation of hydrostatic equilibrium
<b>ICD</b>	inner channel domain
<b>IPCC</b>	Intergovernmental Panel of Climate Change
<b>MISI</b>	Marine Ice Sheet Instability
<b>MISMIP</b>	Marine Ice Sheet Intercomparison Project
<b>OCD</b>	outer channel domain
<b>RMS</b>	root mean square
<b>SIA</b>	Shallow Ice Approximation
<b>SSA</b>	Shallow Shelf Approximation

## 1. Introduction

Ice shelves are the floating tongue extensions of grounded glaciers (ice-sheets) in Antarctica and Greenland. They act as a back-stressing force of grounded ice discharge in the ocean (Fürst et al. 2016; Hughes 1975; Thomas 1973). Enhanced fluxes of ice flow across the transition zone (grounding-line) lead to a decrease of the ice-sheet's mass balance and an increase of the global sea-level budget, as already indicated in the late 70's by Mercer (1978) or later quantitatively calculated and revised by Shepherd et al. (2012). A weakening of the integrity of an ice-sheet/shelf system can be caused by ice-shelf thinning (Bindschadler 2006; Paolo et al. 2015; Pritchard et al. 2012; Wouters et al. 2015) or by the disintegration of the ice-shelf itself (Angelis & Skvarca 2003; Rott et al. 2002). Referring to Antarctica, half of the ice-shelf mass loss can be contributed to basal melt. The remaining other half is linked to the calving of iceberg's (Depoorter et al. 2013; Rignot et al. 2013).

Multiple of these vulnerable ice shelves show longitudinal, sometimes curvilinear features, with length-scales up to hundreds of kilometres and widths of several kilometres (Alley et al. 2016; Drews 2015; Drews et al. 2017). These features can exemplary be shown in Figure 1. Imprinting the shelf-surface with depressions, ice-shelf channels total thickness's can be as thin as half of the total ice thickness of an ice-shelf (Drews 2015) and are linked to sub-shelf geometries with similar shapes. Sensitive modelling of these ice-shelf channels might contribute to a better linkage between enhanced/weakened thinning processes and their impact on ice sheet/ shelf instability.

By using satellite imagery, ground-penetrating radar and radio-echo sounding, several studies pointed out, that these channelised systems may formate at locally varying origins. These can roughly be classified into 'grounding-line sourced' and 'ocean-sourced' channels (Alley et al. 2016). The former can be associated with subglacial-hydrology (Drews et al. 2017; Gourmelen et al. 2017; Jenkins 2011; Le Brocq et al. 2013; Marsh et al. 2016) and/or bedrock perturbations in the vicinity of the grounding line (Drews et al. 2017; Jeofry et al. 2018) and the latter to enhanced sub-shelf melting due to warm Circumpolar Deep Water (CDW). Other previous studies conducted numerical models as e.g. V. Gladish et al. (2012). V. Gladish et al. (2012) consider the ice-ocean interface processes and find melting processes for the Petermann Glacier in Greenland, initiated by channelized morphologies with changing channel widths in the sub ice-shelf. Ensuing research of Dutrieux et al. (2013), Stanton et al. (2013) and Millgate et al. (2013) underpin the hypothesis, that ocean melt can be significantly altered at a channel scale. Furthermore, this is accompanied by Dutrieux et al. (2014b), who finds simple geometries in form of terraces under ice-shelves, where local melting at steeper channel flanks is presumably enhanced. In contrast, flat terraces presumably show constant melt patterns. These patterns, combined with different channel geometries, may influence melt processes on a fine-meter scale.

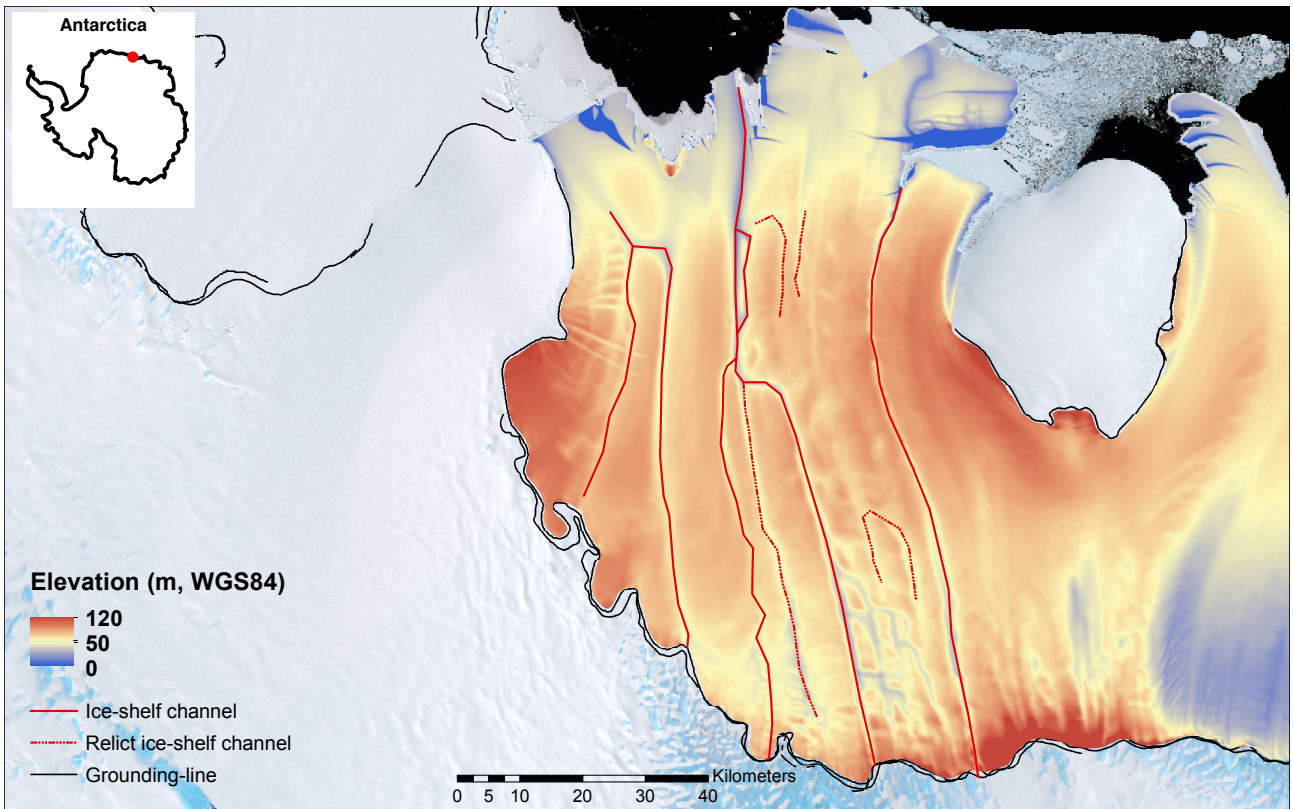


**Figure 1.: Roi Baudouin Ice-Shelf with ice-shelf channels (red, solid), relict features (red, dashed) and grounding-line (black,solid). Surface elevation is based on Berger et al. (2016), grounding line data provided by Rignot et al. (2011), Imagery by Landsat Mosaic of Antarctica (LIMA) Project. Elevation data only for the Roi Baudouin Ice-Shelf depicted. Figure after Drews (2015).**

Summarized, these findings state that narrower, steeper channels might reduce the total amount of melt of the ice-shelf due to a more evenly distributed melt pattern (Millgate et al. 2013; V. Gladish et al. 2012). Beyond that, Drews (2015) addresses, by using a full-Stokes model, that these channel formations can be out of hydrostatic equilibrium. These are noticeably correlated with alternating horizontal shear stresses. As a consequence, relict ridges are sustained at the shelf surface, which might be linked to sedimentary Esker formations near the grounding-line (Drews et al. 2017). Possible relaxation processes, inferred from hydrostatic imbalances are also described earlier by Vaughan et al. (2012). Vertical adjustments in vicinity of ice-shelf channels could then evoke mechanical fracturing and crevassing of channel apexes (Dutrieux et al. 2014b; Sergienko 2013) and furthermore bias local stress patterns (Drews 2015; Vaughan et al. 2012). Conclusively, it seems inevitable to consider full dynamics of an ice-shelf to governing processes, which lower order models might neglect.

Drews (2015) conducts a full-stokes model and accounts for all stress gradients. However, he does not address a potential spatial dependency of varying channel widths on hydrostatic equilibrium. Hence, this might indicate an enhanced or mitigated vulnerability to sub-shelf melting processes (Gourmelen et al. 2017; Mack et al. 2019; V. Gladish et al. 2012) and thus deriving correct shelf thickness's from hydrostatic equilibrium. In a similar way, Vaughan et al. (2012) addressed this problem neglecting any variations of spatially varying channel set-up's.

First and foremost, this thesis aims to improve studies from Drews (2015) by addressing multiple channel geometries with different channel width's to a full-Stokes set-up. The main goal is to analyse the feedback

of hydrostatic imbalances and stress gradients. Furthermore, findings from Drews et al. (2017) and most recently Jeofry et al. (2018) are evaluated. Therefore, a modelling approach tries to reproduce the synthesis of ice-shelf channels, induced by bedrock perturbations near the grounding-line and invoking ice-shelf channels reaching far downstream towards the ice-shelf front. However, the focus of this thesis is not set on melt-initiated processes and does not involve coupled ice/ocean models. Eventually, the emphasis is put on dynamical processes in the interior of the ice-shelf as well as the geometrical changes of the bottom and the top surface by using a noise free synthetic set-up instead.

## 1.1. Objectives

The objective of this thesis is to analyse internal ice-dynamics of an ice-shelf, by using a synthetic set-up. In general, two set-ups are developed. The first set-up treats a 2-D transect of an ice-shelf with instantaneous implemented ice-shelf channels. These channels alter in the channel width. The second set-up treats a 3-D model. Here, the ice-shelf channel is induced by a bedrock uplift at the grounding line. This bedrock uplift is in shape of a three dimensional, symmetric Gauss-function. The following main questions are addressed:

- How does the channel width influence internal ice-dynamics, such as horizontal shear stresses?
- How can these internal dynamics relate to hydrostatic imbalances?
- Do larger domain sizes influence these channel geometries?
- Can a 3-D set-up create channel advection in an ice-shelf and how does this influence the ice-dynamics far downstream of the grounding-line?

## 2. Theory

### 2.1. Governing equations

The full-Stokes equations in glaciology are a system of non-linear partial differential equation (PDE's). They are the most complete description of the flow of ice on a surface and ice, floating on water (Greve & Blatter 2009). They are based on two physical principal, which are the conservation of momentum

$$\underbrace{\nabla P + \nabla \left( \eta(\nabla \mathbf{u} + \nabla \mathbf{u}^T) \right)}_{\nabla \mathbf{T}} + \rho \mathbf{g} = 0 \quad (2.1)$$

and the conservation of mass, as the ice is to be treated as an incompressible fluid:

$$\nabla \cdot \mathbf{u} = 0 \quad (2.2)$$

in which  $\mathbf{u}$  denotes the surface velocities  $u_x, u_y, u_z$  in a three dimensional Cartesian case,  $\eta$  the effective viscosity and  $P$  the pressure. The sum of the pressure gradient and the diffusion term yield the cauchy stress tensor (deviatoric stress tensor). The sum of  $\rho$  and  $g$  denote the hydrostatic force balance. The non-linearity of this set of equations is due to the viscosity of the ice according to Glen's flow law (Glen & Perutz 1955), which is the constitutive law for ice behaviour:

$$\mathbf{T}^D = 2\eta \mathbf{D}, \quad (2.3)$$

where  $\mathbf{T}^D$  is the deviatoric stress tensor resulting from Equation 2.1 and  $\mathbf{D}$  the strain rate tensor.

The ice is assumed to be isothermal and obeys a friction law (weertman sliding law) at its contact surface to ice and the bedrock. The upper ice/atmosphere interface is a moving boundary and satisfies an evolution equation for the height of the ice. To determine the evolution of these two free interfaces, an advection equation of its general form is solved for a kinematic boundary condition:

$$\frac{\partial z_j}{\partial t} + u_x \frac{\partial z_j}{\partial x} + u_y \frac{\partial z_j}{\partial y} - u_z = a_{mb} \quad (2.4)$$

Here,  $a_{mb}$  ( $x, y$  of cartesian coordinate system,  $t$  for timestep) denotes the surface-mass balance or basal-mass balance, partial derivatives of  $z_j$  may either denote surface  $z_s$  or bottom  $z_b$  evolution. The surface ablation/accumulation is prescribed as a vertical component only (Gagliardini et al. 2013). Thus,  $a_{mb}$  denotes the surface and basal mass balance, where  $b$  for subscript  $mb$  prescribes basal melt/accretion  $a_b$  and  $s$  for subscript  $mb$  the surface accumulation/ablation  $a_s$ .

## 2.2. Hydrostatic equilibrium and horizontal shear stress

### Hydrostatic equilibrium

If ice is floating in hydrostatic equilibrium, the total ice thickness  $H$  can be calculated with:

$$H = \frac{\rho_w h_{asl}}{\rho_w - \rho_i} - \frac{\rho_a - \rho_i}{\rho_i - \rho_w} H_a \quad (2.5)$$

where  $\rho_w$  and  $\rho_i$  (Table 1) are the densities for water and ice, respectively. Hence, the hydrostatic thickness  $H$  can be derived from the freeboard height  $h_{asl}$  or the top surface elevation of the domain  $z_s$ . Eventually, the right-hand side term can be neglected, as the inclusion of a firn correction ( $H_a$ ) in the synthetic model set-up is not valid. Equation 2.5 turns then to:

$$H = \frac{\rho_w h_{asl}}{\rho_w - \rho_i} \quad (2.6)$$

This equation is straight-forward, where the hydrostatic thickness can be calculated simply from the modelled top surface  $z_s$ . Equation 2.7 is further used to determine the deviation of hydrostatic equilibrium  $HD$  (also denoted as hydrostatic deviation), which is solely the calculated hydrostatic thickness  $H$  subtracted from the modelled ice-thickness  $z_b$  (Figure 3):

$$HD = H - z_b \quad (2.7)$$

### Horizontal shear stress

For cavity problems (here: ice-shelf channels) the overburden ice-column can lead to shear-stress gradients, transferring the weight to the abutments of the channel, where the weight is fully supported from the bed. This effect is denoted as bridging (van der Veen 2013). To obtain bridging rates for two dimensions of a transect of an ice-shelf or for three dimensions of an coupled ice-sheet/shelf the Cauchy-stress or deviatoric stress tensor (Equation 2.3) is computed from the FS equation, where  $\sigma_{ij}$  denotes nine components for 3-D and 6 for 2-D. Only four of these stress components are different, as the stress tensor itself is symmetrical. Accordingly, this leads to the:

$$\sigma_{ij} = 2\eta \epsilon_{ij} - p \delta_{ij}, \quad (2.8)$$

where the components  $\sigma_{xy}$  and  $\sigma_{yz}$  represent the horizontal shear-stress from subscript  $i, j$  for the 2-D and 3-D set-up, respectively.  $p$  denotes the isotropic pressure. This equation (solver) is implemented in the main-simulation file (see Figure 2). The bridging stress is calculated for the given time-step during the simulation.

### 3. Methods

This chapter introduces a flowchart of the processing chain on the basis of the governing equations explained in chapter 2. This flowchart can be treated as a guideline of the different stages of work (Figure 2). The processing chain includes three major sections. The first part describes prerequisites for the modelling process. These comprise initial thoughts and the main objective of this thesis about the geometry of a synthetic set-up of an ice-sheet/shelf by inducing a basal ice-shelf channel. The second part solely comprises the computational environment, which detailed structure is not further discussed. The third and last part involves the main analysis, which is built upon a self-written, object oriented python-class. This class is described in section 3.2.



**Figure 2.:** Processing chain of applied work flow, which can be subdivided into three major parts, illustrated from top to bottom with different colours. Input geometries depend on the dimensions of the model set-up, which can be 2-D or 3-D. A synthetic geometry is introduced in both cases (see Figure 3 for a schematic illustration). For the 2-D case a ice-shelf transect, for the 3-D-case a shelf/shell set-up after MISMIP (Pattyn et al. (2012)). Geometries are coupled with the main simulation file of Elmer/Ice, containing the suffix .sif. Before initializing and restarting for the transient simulation, the model domain is partitioned to reduce the computational effort (multiple cores are used). The output are large parallel simulation files (for unstructured grids: suffix .pvtu), containing all information, scalars etc. of the simulation. The main conducted analysis is then further customized (rearrangements, merging of partitions, calculations) with the python-class ModelRun.

### 3.1. Model description

All 2-D and 3-D ice sheet/shelf models are set-up within the Elmer/Ice environment, which is an open-source, full-Stokes (FS) ice-sheet/flow model based on the governing equations described in chapter 2. Elmer/Ice provides a broad range of solver-functions, as well as it supports a parallel-computation environment, by solving the full-Stokes equations for specific ice-rheologies.

The Elmer/Ice main simulation file (Figure 2) includes a set-up of bodies with a specific material property, which define ice, water and surfaces. A specific body force acts on each body. Body forces are in general the gravitational acceleration ( $g$  in Figure 3), as well as lower and upper accumulation/ablation/melt fluxes (detailed description in the following sections). The employed model comprises the free top and lower surface, as well as the ice itself for different material properties. Each component denoted as a body, is subject to a body force. Boundary conditions (BC) are applied at the shelf front, sides, lower and free surface (Figure 3), also containing parallel flow BC's. Here, perpendicular ice velocity is zero at the domain boundaries for the lateral constraints in 2-D and 3-D. Note that the declaration of the coordinates is different for 3-D and 2-D. The vertical axis for the 3-D axis is denoted as  $z$ . The 2-D vertical axis is denoted as  $y$ . The detailed description for both, the 2-D and 3-D model set-up can be found in subsection 3.1.1 and subsection 3.1.2, respectively.

Table 1 denotes all important parameters with their respective values. The parameter set-up is for the 2-D and 3-D model slightly different. The 2-D model is assumed to be more idealized, representing a pure transect of an ice-shelf. Thus, the implementation of the friction parameter  $C$  for Weertman's sliding law is not necessary. The used densities for water and ice neglect any air-bubble intrusions or freshwater perturbations, resulting in real ice densities of  $910 \text{ kg m}^{-3}$ . In contrast, implemented densities of the 3-D model are more real-world applicable (account for air in ice or freshwater storages), by using a smaller ice  $\rho_i$  and fresh-water  $\rho_w$  density. The time increment describes the size of one timestep.

**Table 1.:** *Physical quantities with their respective units used for the transient simulations in 2-D and 3-D model set-up within Elmer/Ice.*

Quantity	Value (2-D set-up)	Value (3-D set-up)	Unit
Length of year, $1 \text{ a}$	3 155 760 000	3 155 760 000	$s$
Time increment	0.5	0.5	-
Density of ice, $\rho_i$	910	900	$\text{kg m}^{-3}$
Density of freshwater, $\rho_w$	1000	1000	$\text{kg m}^{-3}$
Density of ocean-water, $\rho_o$	1025	-	$\text{kg m}^{-3}$
Surface accumulation, $a_s$	0.3	0.3	$m a^{-1}$
Basal melt, $a_b$	0.3	-	$m a^{-1}$
Gravitational acceleration, $g$	9.81	9.81	$m s^{-2}$
Power law exponent, $n$	3	3	-
Ice softness, $A$	$3.3 * 10^{-5}$	$4.6 * 10^{-25}$	$\text{Pa}^n s^{-1}$
Viscosity, $\eta$	$\frac{1}{2A}^{1*n^{-1}}$	$\frac{1}{2A}^{1*n^{-1}}$	$\text{kg m}^{-1} s^{-1}$
Gas constant, $R$	8.314	8.314	$\text{kg m}^2 s^{-2} mol^{-1} K^{-1}$
Activation energy, $Q_1$	60	60 for $T' \leq 263.15 \text{ K}$	$\text{kJ mol}^{-1}$
Activation energy, $Q_2$	139	139 for $T' \geq 263.15 \text{ K}$	$\text{kJ mol}^{-1}$
Friction parameter, $C$	-	$7.624 * 10^6$	$\text{Pa m}^{-1/3} s^{1/3}$

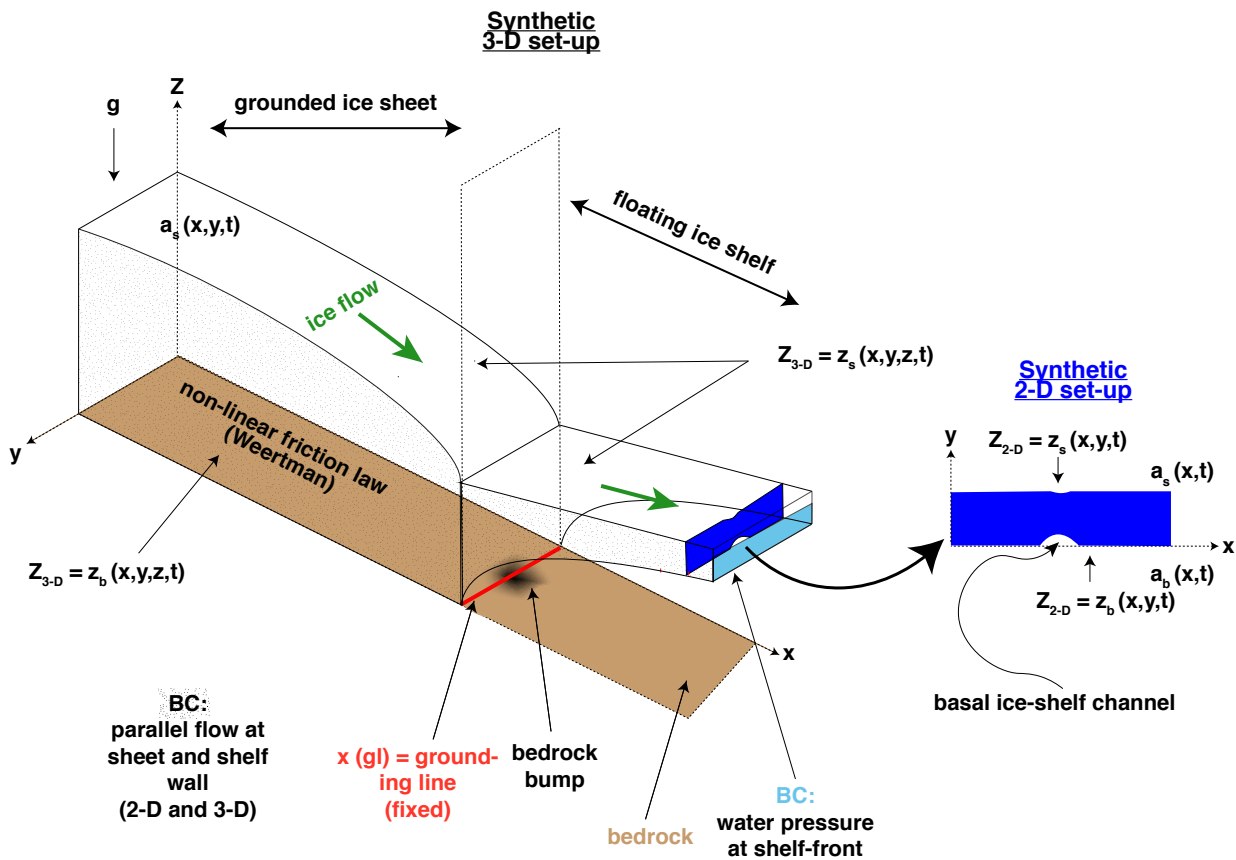


**Figure 3.: Schematic overview of the 3-D and 2-D model set-up.** Depicted are a fully coupled 3-D ice-sheet/shelf model with a 2-D transect of an ice shelf. The initialization of an ice-shelf channel for the 2-D set-up is as follows: 2-D Gaussian-bell curve for the lower surface at ( $Z_{2-D} = z_b$ ). For the 3-D set-up: bedrock bump at position of the grounding line position (no initial perturbation of ice;  $Z_{3-D} = z_b(x(gl))$ ). The dotted plane divides the grounded from the floating part. The transient surface  $Z$  is equal to  $z_b$  (note:  $Z_{3-D} = z_b$ , which entails the bedrock for the ice-sheet in the 3-D set-up with a non-linear friction law) and  $z_s$  for the free top surface. The accumulation and ablation terms for free top and bottom surface are denoted as  $a_s$  and  $a_b$  for the 2-D model. For the 3-D model as follows: solely surface accumulation  $a_s$ . The boundary conditions for the 3-D case describe parallel flow at the constraints of ice-shelf and sheet. Water pressure is applied at the front and beneath the ice-shelf. For the 2-D case, the boundary conditions are almost equal to the 3-D case. However, a second force is applied at the lateral constraints (hydrostatic force).

### 3.1.1. Synthetic 2-D ice-shelf set-up

The model geometry in the 2-D case is a two dimensional rectangle, as a transect of an ice-shelf with a comparable height and width of an ice-shelf. For simplifications, prescribed values for the surface and the basal mass-balance are equal (Table 1). The implemented structured grid is a regular quad-mesh without any grid refinement. The initialisation of the basal ice-shelf channel (Figure 3) is induced as an instantaneous gauss function for the lower surface  $z_b$ , multiplied with the ratio of the density of ocean water  $\rho_o$  and ice  $\rho_i$  as follows:

$$z_b(w_{mod}, h_{ch}) = \frac{1 - \rho_i}{\rho_o} h_{ch} \exp \frac{-(x-x)}{w_{mod}}. \quad (3.1)$$

In Equation 3.1  $h_{ch}$  describes the uniform channel-height and  $w_{mod}$  the model's channel width and input value. The value of  $x$  describes the position of the channel apex. The channel apex is for all model runs at the exact half of the domain size (Figure 12). The channel does not shift laterally. For simplifications, the translation from  $w_{mod}$  to  $w_{real}$  is done with  $w_{real} = \sqrt{w_{mod}} * 4$ . Here,  $w_{real}$  describes the original channel width on a meter scale. This value is used in the results part. The value of  $w_{mod}$  is only important for the ModelRun.py class as an input parameter. In general, parameters which are subject to change are thus the channel width  $w_{mod}$  or  $w_{real}$ , respectively. In chapter 4 and corresponding figures,  $w_{real}$  will be named cw (channel width). Note, that the geometry of the bottom interface is only changes for the channel width and not for the channel height.

The channel width varies between  $x_{realmin} = 126$  m and  $x_{realmax} = 3794$  m and has a constant channel height  $h_{ch} = 150$  m (Appendix C). In total, 34 model-runs were executed for regular domain sizes with different channel width as follows:  $1 * 10^3 - 9 * 10^3$ ,  $1 * 10^4 - 9 * 10^4$ ,  $1 * 10^5 - 9 * 10^5$ ,  $1 * 10^6 - 9 * 10^6$ . These are the dimensionless channel-widths for  $w_{mod}$ . For example:  $1 * 10^3$  is equal to 126 m. The regular domain size is 20 km x 0.304 km as depicted in Table 4. Model runs from  $10^4 - 90^4$  are also executed with two wider domains in x-direction (lateral shelf extent); an extended domain with 40 km (doubled-size) and an extra-extended domain with 100 km (5x of original domain). The amount of cells in x-direction are doubled (666x15) and multiplied by 5 (1665x15) for the latter case, respectively. Therefore, runs with an extended and wide-extended domain have the similar name with the suffix 'extended' and 'wide\_extended' (e.g. CH894\_2D\_extended). The ice shelf height  $H$  remains for all cases (see Table 4). For the 2-D case Equation 2.4 term  $u_y \frac{\partial z_j}{\partial y} = 0$  and the vertical surface velocity  $-u_z$  is written as  $-u_y$  (see coordinate system in Figure 3 for 2-D set-up).

As depicted in Figure 4, the left and right hand side of the Gaussian bell curve is defined as the channel flanks. The highest point of this curve describes the channel apex or the original channel peak, which equals  $h_{ch} = 150$  m.

**Table 2.:** A summary of the 2-D model set-up, with the first set of model-runs. The table depicts the name of the model-run, the width used with Elmer/Ice ( $w_{mod}$ ), the translated width ( $w_{real}$ ), the size of the domain ( $x_{dom}$  and  $y_{dom}$  extent). The vertical extent  $y_{dom}$  is calculated with  $\rho_i$  and  $\rho_w$  from Equation 2.5. Note: \*\* signs runs, which have been executed for both, extended and wide-extended domains (more in Appendix C).

Name	Channel dim. ( $w_{mod}, w_{real}$ )	Domain dim. ( $x_{dom}, y_{dom}$ )	Timespan	Cells ( $x, y$ )
...				
CH400_2D**	10000, 400 m	20 km x 0.304 km	1000 a	333x15
CH566_2D**	20000, 566 m	20 km x 0.304 km	1000 a	333x15
CH692_2D**	30000, 692 m	20 km x 0.304 km	1000 a	333x15
CH800_2D**	40000, 800 m	20 km x 0.304 km	1000 a	333x15
CH894_2D**	50000, 894 m	20 km x 0.304 km	1000 a	333x15
CH980_2D**	60000, 980 m	20 km x 0.304 km	1000 a	333x15
CH1058_2D**	70000, 1058 m	20 km x 0.304 km	1000 a	333x15
CH1132_2D**	80000, 1132 m	20 km x 0.304 km	1000 a	333x15
CH1200_2D**	90000, 1200 m	20 km x 0.304 km	1000 a	333x15
...				

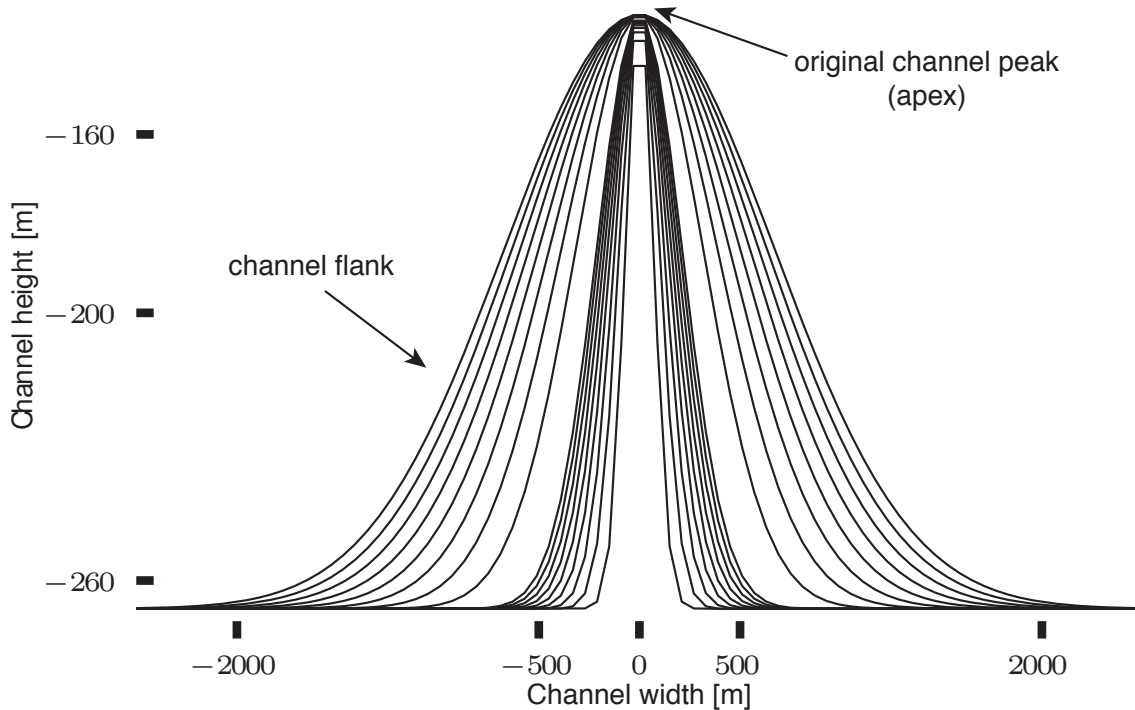


**Figure 4.:** Summary of all channel widths included in the 2-D model. The x-axis describes the alternating channel width ( $w_{trans}$ ), the y-axis describes the uniform channel height ( $h_{ch}$ ). Note: very narrow channels might alter in channel height, if they are smaller than grid resolution.

### 3.1.2. Synthetic 3-D coupled ice-sheet/shelf set-up

The initialisation of the 3-D model is based on the inter comparison project for marine ice-sheets: MISMIP (eg. Pattyn et al. (2012), Gagliardini et al. (2016)). The model neglects thermal effects and grounding line dynamics (here: the model set-up has a fixed and stable grounding-line and does not move forward or backward), the ocean pressure is applied at the bottom and front of the ice-shelf (Figure 3). In addition,

a time-dependent scheme for the whole interface elevation is applied, as a small hydrostatic imbalance causes large geometrical changes due to high vertical velocities (Durand et al. 2009). The channel is initiated by perturbation directly at the grounding line position  $x(\text{gl})$  (Figure 3). The perturbation simulates a bedrock-uplift up to 50 years (the bump is in shape of a three dimensional, symmetrical Gauss function – comparable with the 2-D case) starting at  $t = 0$  (see Equation 3.2). The transient bump-perturbation is implemented in the main file as an additional body force acting on the bedrock. The grounding line describes the transition from vertical shear dominated to a longitudinal membrane stress flow. Hence, to obtain proper results and to avoid erroneousness, it is mandatory to refine the grid in this transition zone. As the channel evolves and starts at the GL, the grid is in  $x(\text{gl})$  (across flow direction) and  $y$  (along flow direction) extent refined (Dias dos Santos et al. 2018; Gagliardini et al. 2016). Hence, an unstructured mesh is used, which relies on a delaunay triangulation. The final channel height  $h_{ch}$  after 50 years is for all considered model runs 250 m. Equation 3.2 explains the channel induction in a 3-D Cartesian coordinate system:

$$z_b(w_{xy}, h_{ch}) = \left( \frac{t}{50} \right) h_{ch} \exp \frac{-(x - x_0)^2}{(w_{xy})^2} + \frac{(y - y_0)^2}{(w_{xy})^2}, \quad (3.2)$$

where  $t$  is the timestep,  $h_{ch}$  the constant channel height with 250 m in  $z$  direction,  $w_{xy}$  is the extent in  $x$ - and  $y$ -direction, respectively. This bump extent is for  $x$ - and  $y$ -direction identical. Thus, a uniform value  $w_{xy}$  applies for both,  $x$ - and  $y$ -direction. The regular variables  $x$  and  $y$  define the coordinates. The values for  $x_0$  and  $y_0$  define the initial position of the bump apex in a three dimensional coordinate system. Furthermore,  $x_0$  is equal to the grounding-line position  $x(\text{gl})$  as depicted in Figure 3 and  $y_0$  is set to zero (half of the domain size). The bump stops growing when  $t = 50$ .

**Table 3.: A summary of the 3-D model-setup, with the main set of model-runs.** The table depicts the name of the model-run, the width used with Elmer/Ice ( $w_{xy}$ ) which is the real-width for all 3-D simulation, the size of the domain  $x_{\text{dom}}$ ,  $y_{\text{dom}}$  and  $z_{\text{dom}}$ . Note:  $z_{\text{dom}}$  is the maximal height of the ice-sheet.  $x_{\text{dom}}$  and  $y_{\text{dom}}$  are the lateral and longitudinal extent, respectively. All runs simulate an ice-sheet/shelf evolution of 200 years.

Name	Channel dim. ( $w_{xy}$ )	Domain dim. ( $x_{\text{dom}}, y_{\text{dom}}, z_{\text{dom}}$ )	Timespan
CH100_3D	100 m	10 km x 70 km x 1.3 km	200 a
CH150_3D	150 m	10 km x 70 km x 1.3 km	200 a
CH200_3D	200 m	10 km x 70 km x 1.3 km	200 a
CH250_3D	250 m	10 km x 70 km x 1.3 km	200 a
CH300_3D	300 m	10 km x 70 km x 1.3 km	200 a
CH400_3D	400 m	10 km x 70 km x 1.3 km	200 a
CH450_3D	450 m	10 km x 70 km x 1.3 km	200 a
CH500_3D	500 m	10 km x 70 km x 1.3 km	200 a
CH550_3D	550 m	10 km x 70 km x 1.3 km	200 a
CH600_3D	600 m	10 km x 70 km x 1.3 km	200 a
CH800_3D	800 m	10 km x 70 km x 1.3 km	200 a
CH900_3D	900 m	10 km x 70 km x 1.3 km	200 a
CH950_3D	950 m	10 km x 70 km x 1.3 km	200 a
CH1000_3D	950 m	10 km x 70 km x 1.3 km	200 a
CH1200_3D	1200 m	10 km x 70 km x 1.3 km	200 a
CH1400_3D	1400 m	10 km x 70 km x 1.3 km	200 a

### 3.2. Data processing

The computational environments of fluid dynamics are usually similarly structured. One of those typical workflows is also depicted in Figure 2 and is part of this thesis. At a certain post-processing stage, a user usually got a wide variety of tools to visualize and arrange the output of the conducted model. These programs might be useful for a quick visualisation, but are often not capable of handling and visualising a great number of similar plots, as well as the most graphical user interfaces are quite slow.

In order to perform numerous calculations of the same degree with numerous simulation outputs, a small python package is developed. This package contains a class called **ModelRun** and provides several methods. These methods are built to

1. extract large parallel simulation files with unstructured and structured grids of the format `.vtu`, which are VTK XML file-types
2. apply numerous methods (extract any information about a number of cells, scalars etc., calculate hydrostatic thicknesses, extract concave hulls, merge partitions or cut 3-D model domains)
3. and transform the extracted data to a numpy format to make plottable arrays or matrices

The used cross-platform *VTK* predominantly built upon the C++ class library and unfortunately is not very well documented for python users. This class might be helpful for future work in the ESD research group or any other user when dealing with 2-D or 3-D modelling outputs with VTK file format. Furthermore, the class is easily transferable and open for modification and adjustments.

## 4. Results

The following chapter provides subsections with an overview of selected benchmark model runs with two characteristic channel widths (1 x narrow = CH894\_2D and 1 x wide = CH1264\_2D), which depict the deviation of hydrostatic equilibrium (HD) for two given time-steps (50 and 200 years). The HD is then compared with the computed horizontal stresses of the cauchy stress tensor (from Equation 2.8) and the vertical flow velocities within the regular channel domain. In addition, the channel's calculated hydrostatic thickness and its geometry itself is analysed. The maximum channel peak deviation, as well as the deviation of channel abutments (Figure 5) are compared with the root mean square (RMS) of the HD of the whole domain. Eventually, three different domain extents are modelled with equal channel widths to evaluate their correlation and impact on the total HD and its dependency of alternating channel widths.

### 4.1. Deviation of hydrostatic equilibrium (HD)

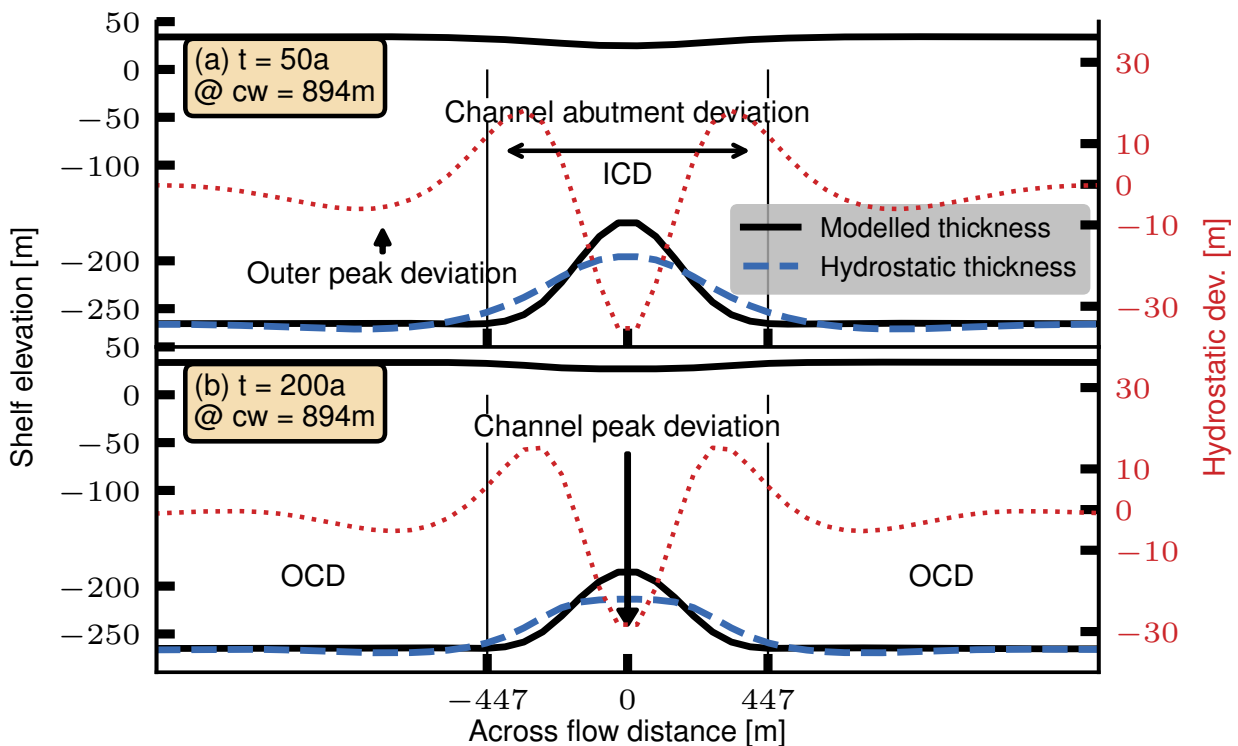


**Figure 5.:** Deviation of hydrostatic equilibrium (dotted, red), it's corresponding modelled thickness for  $z_b$  and  $z_s$  (black, solid) and calculated hydrostatic thickness of the upper surface (blue, dashed), where **(a)** is after 50 and **(b)** after 200 years. The y-axis is separated into the shelf elevation and the deviation of hydrostatic equilibrium for left hand side and right hand side, respectively. The x-axis depicts the lateral extent of the channel ( $cw = 894$  m) where major-ticks annotate the channel's half-width and center. Left and right of the black, solid vertical lines: outer channel domain (OCD); in between: inner channel domain (ICD).

Figure 5 depicts a benchmark run of  $cw = 894$  m for the 2-D simulation case for two timesteps. The upper plot (a) is after 50 years, whereas plot (b) is after 200 years. The first y-axis (left, black) holds the absolute shelf elevation which is plotted against the channel width. The major ticks of the x-axis annotate the channel's half width. The secondary y-axis (right, red) holds the deviation of hydrostatic equilibrium (HD), which corresponds to the red, dotted line plot. For latter figure descriptions prominent features of HD are treated separately. The channel peak deviation is one of the most crucial features among the HD line plot. The channel peak deviation depicts its absolute maximum at  $x=0$ . The HD is approximately -32 m for (a) and -28 m for (b) at  $x=0$ . Other prominent features are the channel abutments in Figure 5, which describe the HD of the channel flanks. On the left and right hand side of the outer channel domain (OCD) (the area of the domain, where the gradient of the modelled thickness is zero), the HD shows another minor variation until it levels off at  $y=0$ .

#### 4.1.1. Flow velocities

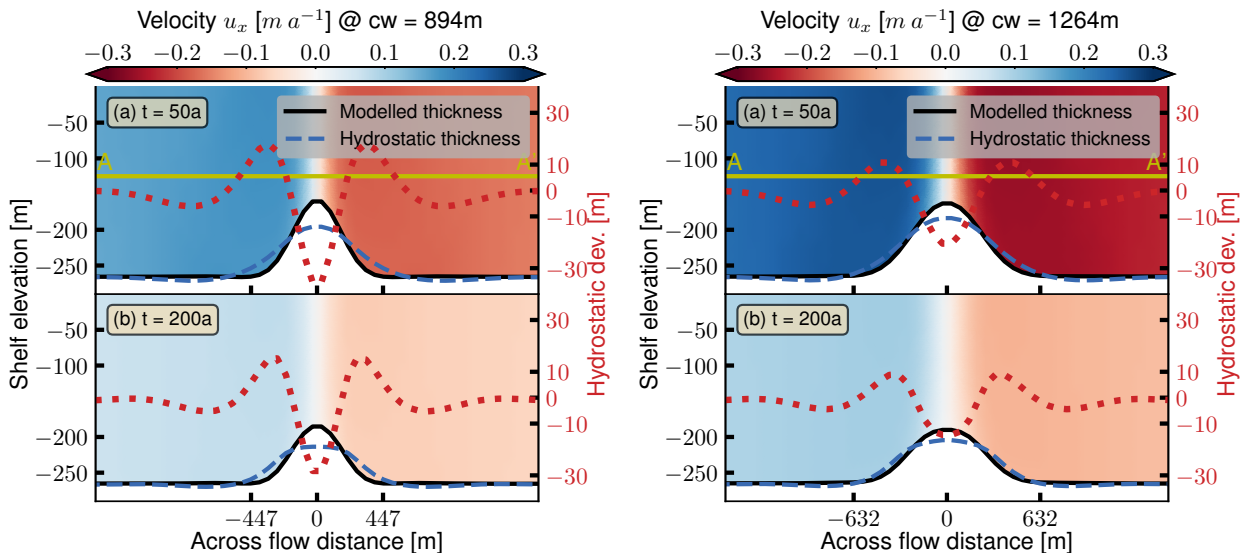


**Figure 6.:** Horizontal ice shelf flow-velocities in  $x$ -direction with  $u_x$  for the 2D simulation case. Two channel widths with 894m (left) and 1264m (right), both at two different timesteps: (a) = 50 years, (b) = 200 years. Line plots: modelled thickness (black, solid), calculated hydrostatic thickness (blue, dashed) and HD. Higher flow velocities for (a) and wider channel ( $cw = 1264$ ) as for (b). Cross sections A-A' can be found in Figure 8.

Figure 6 depicts the two benchmark runs for  $cw = 894$  m as the narrow channel and  $cw = 1264$  m as the wide channel. Similar to Figure 5, the y-axis shows two scales, where  $y_1$  (left, black) depicts the shelf elevation and  $y_2$  (right, red) the HD. Both share the x-axis with an absolute domain length of 3 km with their respective channel half widths, annotated with major ticks. The OCD of the left channel sides depicts negative flow velocities, the OCD of the right channel side depicts positive flow velocities. The flow velocities in (a) for the narrower channel are smaller than for the wider channel. For  $x=0$  flow velocities are zero and start to distribute equally in OCD. The wider channel's HD after 50 and after 200 years is noticeably smaller than for the narrower channel at the channel peak deviation. The outer peak deviation for both channel widths are considerably smaller.

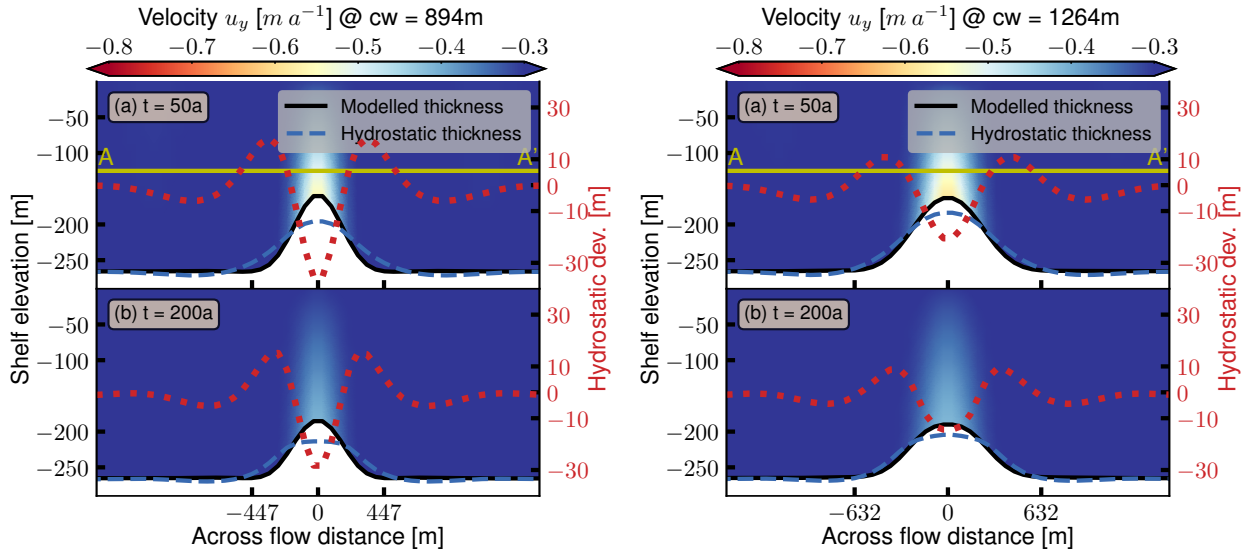


**Figure 7.:** Vertical ice-shelf flow-velocities in  $y$ -direction with  $u_y$  for the 2-D simulation case. Two channel widths with 894 m (left) and 1264 m (right), both at two different timesteps: (a) = 50 years, (b) = 200 years. Line plots: modelled thickness (black, solid), calculated hydrostatic thickness (blue, dashed) and HD. All: Higher vertical flow velocities towards channel peak. Narrow and wide channel compared: Higher vertical flow velocities for wider channel than for narrower channel.

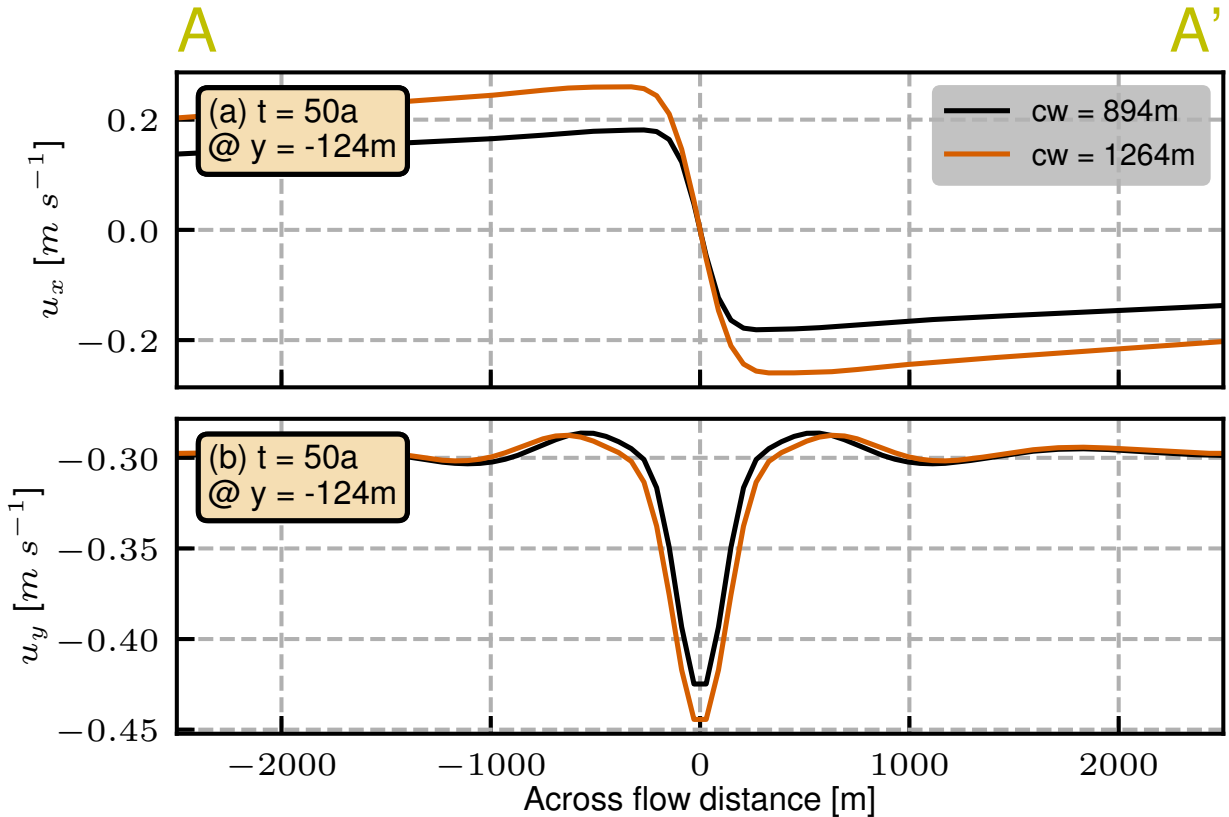


**Figure 8.:** Ice shelf flow-velocities as a profile at  $y = -124$  m (see Figure 7 profile) shelf elevation for the 2-D simulation case. (a) shows  $u_x$  for two channel widths with 894 m (black) and 1264 m (orange) with  $t = 50$  years. Prominent velocity step, when reaching the ICD. (b) shows  $u_y$  with similar channel widths and timestep.

The line plots (modelled thickness, hydrostatic thickness and HD) of the subplots of Figure 7 are identical to those which are shown in Figure 6. However, the vertical flow velocity  $u_y$  reaches its maximum (negative flow velocities) at  $x = 0$ , which is at the coordinate of the absolute maximum peak deviation. The magnitude of the velocity pattern diminishes towards the channel flanks and reaches its minimum within the OCD. This is valid for both, the wide and also the narrow channel. In y-direction, the channel velocities decrease with an increasing elevation (from  $z_b$  to  $z_s$ ).

The profile plots in Figure 8 confirm, that horizontal velocities (a) reach their absolute maxima at the channel abutment deviation (see Figure 5). However, the function is then linearly decreasing, whereas the magnitude of the two velocity functions is different, the gradient remains equal over the whole domain, for both  $cw = 894$  m and  $cw = 1264$  m. The horizontal velocity profiles are point symmetrical to the origin of the coordinate system. In Figure 8 (b), vertical flow velocities do not differ in the OCD. They tend to oscillate with decreasing distance to the centre of the domain. Shortly after the ICD is passed, the absolute velocities are increasing sharply with a linear slope. The difference of vertical velocities between  $cw = 894$  m and  $cw = 1264$  m is minimal. Nonetheless, the wider channel shows slightly higher absolute velocities than the narrower channel.

#### 4.1.2. Horizontal shear stress

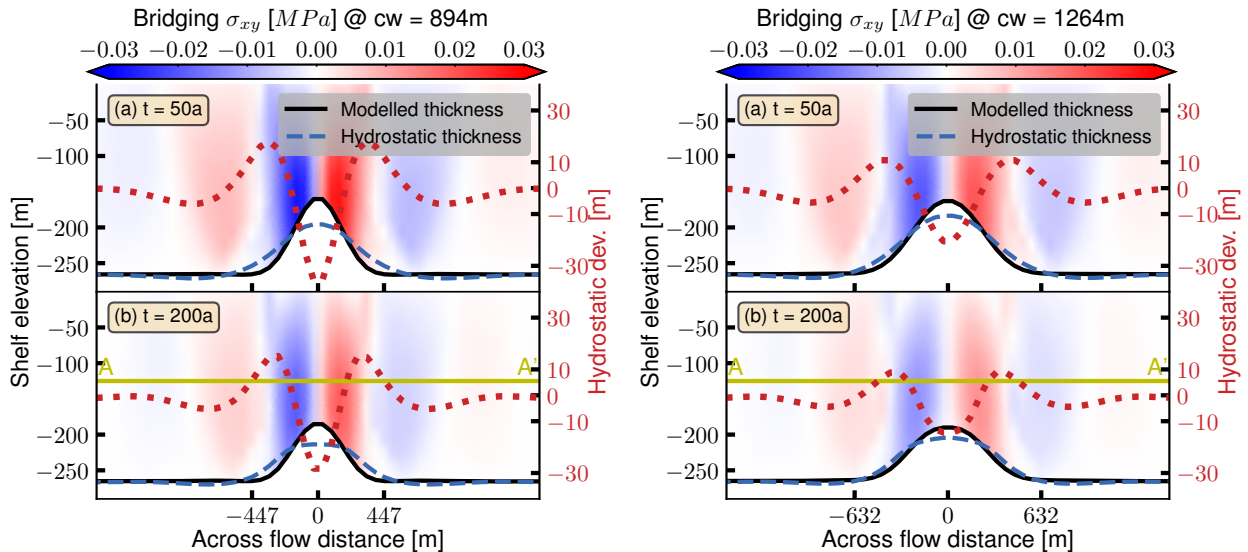


**Figure 9:** Horizontal shear stress  $\sigma_{xy}$  for the two benchmark runs with  $cw = 894$  m (left) and  $1264$  m (right). Timestep for (a) = 50 years, for (b) = 10 years.  $\sigma_{xy}$  with highest values within the narrow channel, whereas the wider channel has less horizontal shear stress. With increasing time, the horizontal shear stress starts to diminish. A and A' are cross sections for the bridging pattern for a narrow and a wide channel width (Figure 10).

Horizontal shear stress also referred as the deviatoric stress or bridging, shows a clear pattern of the ice-shelf cross-section for the narrow and the wide channel in Figure 9 with a negative axial symmetry. Highest values are obtained, where the channel flanks are located. The horizontal distribution of the shear stress diminishes within the OCD. The vertical distribution predominantly shows a regular pattern with a constant horizontal shear stress. Along x-direction, the bridging patterns fluctuates between negative and

positive values, whereas the absolute maximum values 0.003 MPa and minimum values 0.001 MPa are subject to the ICD and OCD, respectively. For the narrow channel benchmark run, bridging stresses are noticeably higher than for the wide channel benchmark run.

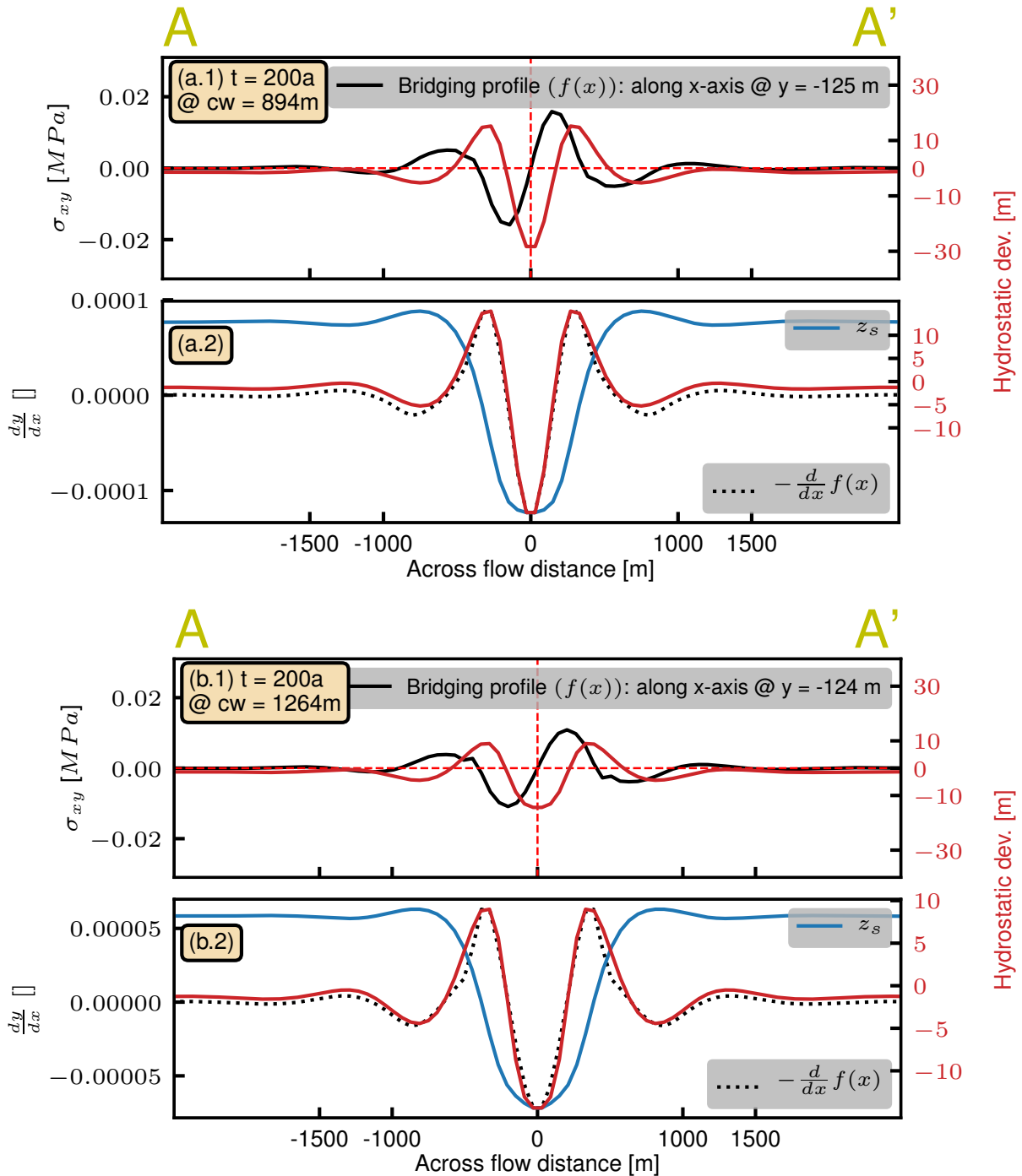


**Figure 10.: Subplots for bridging profiles  $f(x)$  of Figure 9 (A-A' for  $cw = 894$  m and  $cw = 1264$  m). HD (red, solid) with a supplement of the derivative of the profile function  $f(x)$ . (a) depicts a narrow channel simulation with  $cw = 894$  m. (b) depicts a wide channel simulation with  $cw = 1264$  m. (a.2) and (b.2) depict also the top surface  $z_s$  for given the given width (superelevated and without labelled axis). (a.2) and (b.2) show the first negative derivative of the bridging profile (superelevated and dimensionless) at  $y = -125$  m and  $y = -124$  m, for CH894\_2D and CH1264\_2D, respectively. The gradients of the negative derivative match the gradient of the HD. Note: this is not valid for absolute values.**

In the following, the focus is put on the comparison of the function  $f(x)$ , which describes the bridging profile for given x-values across the flow direction with the HD (a.1, b.1). Furthermore, a derivative of the plotted bridging profile is calculated with regard to the HD. The first negative derivative is plotted with the HD (a.2, b.2). The equation for the numerical differentiation can be found in Appendix B.

Figure 10 is linked to Figure 9 and emphasizes the relationship between the HD and the horizontal shear stress of the ice-shelf transect. The chosen profiles of the bridging stresses are located slightly above the channel peak at  $y = -125$  m for the narrow channel and  $y = -124$  m for the wide channel. The bridging profile is denoted as  $f(x)$ . In order to match the gradient, the calculated derivative is dimensionless and scaled.

The slope of  $-\frac{d}{dx} f(x)$  matches the slope of the hydrostatic deviation (Figure 10; a.2 and b.2). This result is valid for the run CH894\_2D, which benchmarks the narrow channel and CH1264\_2D which benchmarks the wide channel. In addition, the top surface  $z_s$  shows two peaks separated by a depression. The depression matches the depression of the HD and the negative derivative of  $f(x)$ . The two peaks of the HD and the negative derivative of  $f(x)$  correspond to the steepest slopes of the the top surface  $z_s$ . Calculated derivatives of  $z_s$  of all model-runs can be found in Appendix C.

#### 4.1.3. Abutment and channel peak deviation

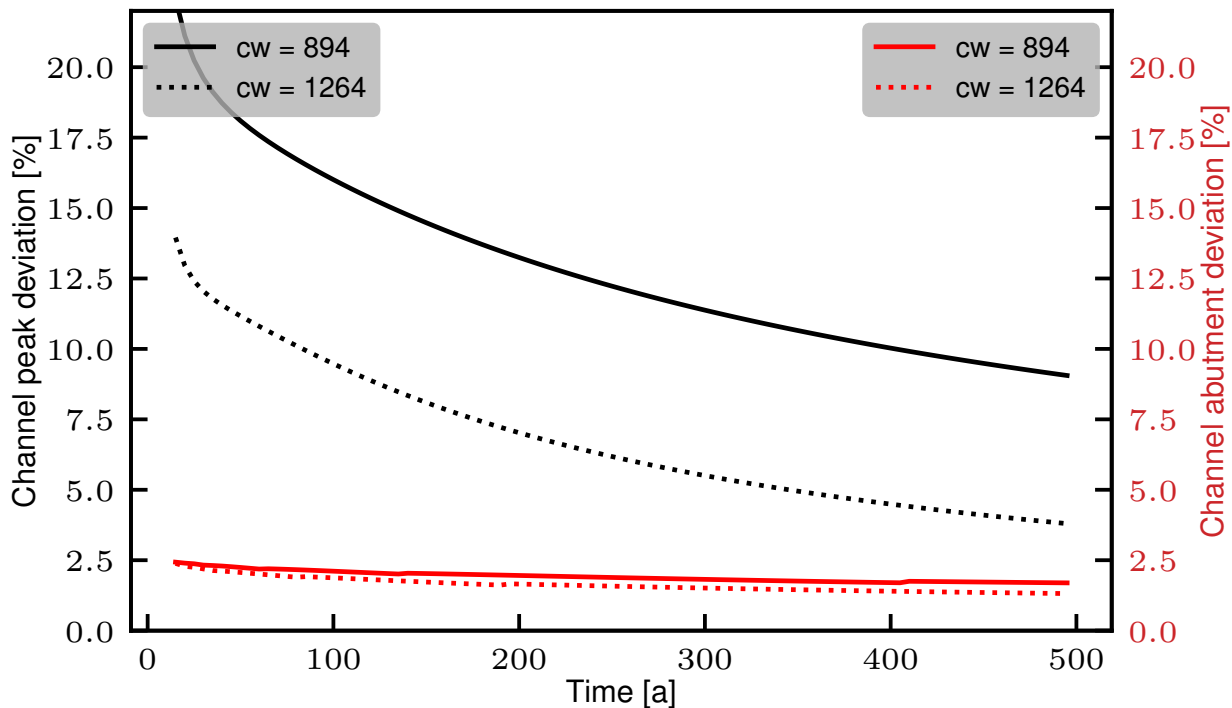


**Figure 11.: Channel peak and abutment deviation with a relative deviation for a narrow ( $cw=894$  m) and a wide ( $cw = 1264$  m) channel width. The left y-axis depicts the channel peak and right y-axis channel abutment deviation. In general, the decrease of the relative channel peak deviation exponentially consistent, whereas the relative channel abutment deviation depicts a rather constant or linear slope.**

Figure 11 depicts the relative channel peak deviation ( $y_1$ , left, black) and the relative channel abutment deviation ( $y_2$ , right, red). The channel peak deviation diminishes within the first 100 years with a exponential slope until it flattens during the following 400 years. These two phases of decrease can be shown for CH\_894\_2D and CH\_1264\_2D. However, the HD of CH\_894\_2D reaches after 500 years approximately 3% to 4%, whereas CH\_1264\_2D is about 5% higher.

The channel abutment deviation is significantly lower than the channel peak deviation. After 100 years the wide channel  $cw = 1264$  m shows a relative channel peak deviation of approximately 17.5%, whereas the channel abutment deviation reaches values slightly under 2.5%. The slope of the latter (decrease of relative channel abutment deviation) is almost neglectable. It starts at 2.5% and slowly diminishes to 2%. In summary, the channel abutment deviation is significantly smaller for the first years (more than 20% difference) than the relative channel peak deviation. However, after 500 years it is noticeable, that the relative abutment deviation reaches a steady state, because no more changes are observed. In contrast, the relative channel peak deviation is decreasing exponentially, towards a similar relative deviation as the channel abutment. The explanation and equation for the numerical differentiation can be found in Appendix B.

#### 4.1.4. Correlation of channel width with deviation of hydrostatic equilibrium

In the following, Figure 12 depicts numerous runs of the conducted simulations, which are arranged and plotted with respect to the channel width on the x-axis. The left y-axis ( $y_1$ , left, black) considers the root mean square (RMS) of the HD of each single run at a given timestep, by considering the total lateral extent of the regular domain (20 km). The used equation can be found in Appendix B. The second axis ( $y_2$ , right, red) denotes the channel peak deviation. The RMS and channel peak deviation is calculated for runs with regular, extended and wide-extended domain.

As a result of Equation B.1 (Appendix B), the RMS of the HD ( $y_1$ , Figure 12) is not a subject of change from (a) to (d). All timesteps depict a minimum of the RMS of the HD of approximately 1.9 m as a threshold. The total difference of the curve change with increasing timesteps is minor. However, the channel peak deviation (red) shows a clear trend towards no peak deviation with increasing channel width and increasing time. Figure 12 shows a vertical decreasing function of the channel peak deviation with increasing time.  $Y_1$  and  $y_2$  axis have not the same scale (10m to 0m and 40 m to 0 m, respectively). As a result, the absolute channel peak deviation is always higher than the RMS of HD.

When comparing both, the RMS of hydrostatic deviation and the channel peak deviation with the increasing channel width, there is a significant (linear) decrease for smaller channel widths from approximately 8 m to 1 m. For wider channels one can observe no major decrease or increase. Especially wider channels at  $t = 200a$  and  $t = 250a$  converge to zero deviation for the channel peaks. Regardless, the shape of the plotted functions can be described as exponential. Additionally, a crucial flattening between 500m and 1500m is observed over time from  $t = 20a$  to  $t = 250a$ .

The different channel domain extents (regular, extended and wide-extended) show no major differences when they are compared with each other (dotted and dashed lines are predominantly not noticeable). It follows that the deviation of the hydrostatic equilibrium is equal for all extents.

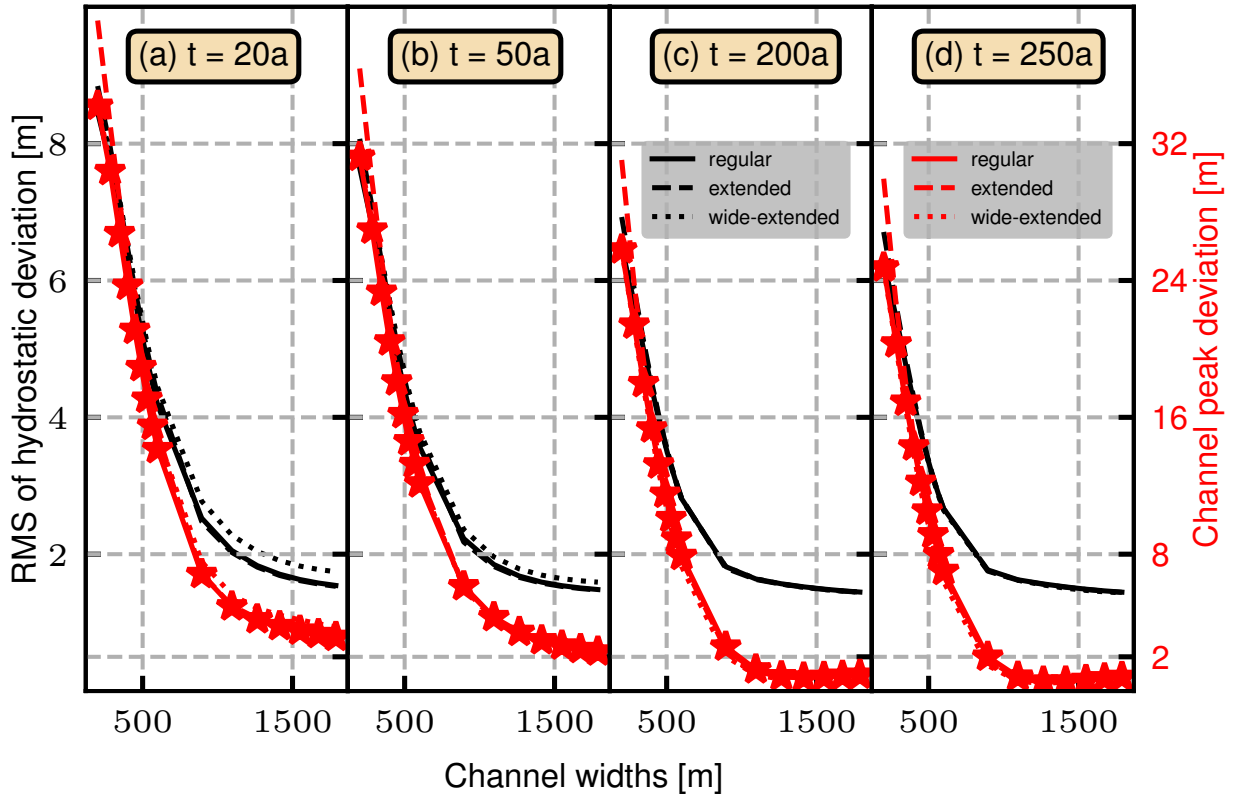


**Figure 12.**: RMS of HD and channel peak deviation vs. increasing channel width for four different timesteps: (a) = 50 years, (b) = 200 years (c) = 400 years, (d) = 500 years. Every subplot depicts the RMS of HD for 60 model runs (20 runs for each domain size: regular, extended and wide-extended) for  $y_1$  (left, black). The channel peak deviation is plotted on the right y-axis in red.

#### 4.1.5. Influence of the domain size on channel closing

Former sections of the results chapter explain the influence of different channel widths on the hydrostatic equilibrium as well as on flow velocities and horizontal shear stresses. This subsection treats the behaviour of the real channel with its peak amplitude and how its geometry compares to equal runs with the same parameter set-up, but with an extended domain size. We analyse the sensitivity of three lateral extended domains (subsection 3.1.1) on channel closing with different channel widths.

Figure 13 depicts the elevation of the channel peaks (for all runs at  $x=0$ , apex) and its time dependency for  $y$ - and  $x$ -axis, respectively. The elevation of the bottom channel peak is successively non-linearly decreasing over time for all domain sizes and all channel widths. The decrease of the channel peak starts at approx. -150 m and goes below -210 m for wider channels. Channels embedded in the two wider domains (extended and wide-extended) show faster closing rates. Furthermore, wider channels show faster closing rates than narrower channels as well (see regular-domain end-point of simulation in (a) and (d), where (a) is well above and (d) under -210 m). Note, that for the second row ((d),(e),(f)) no runs for the extended domain were executed.

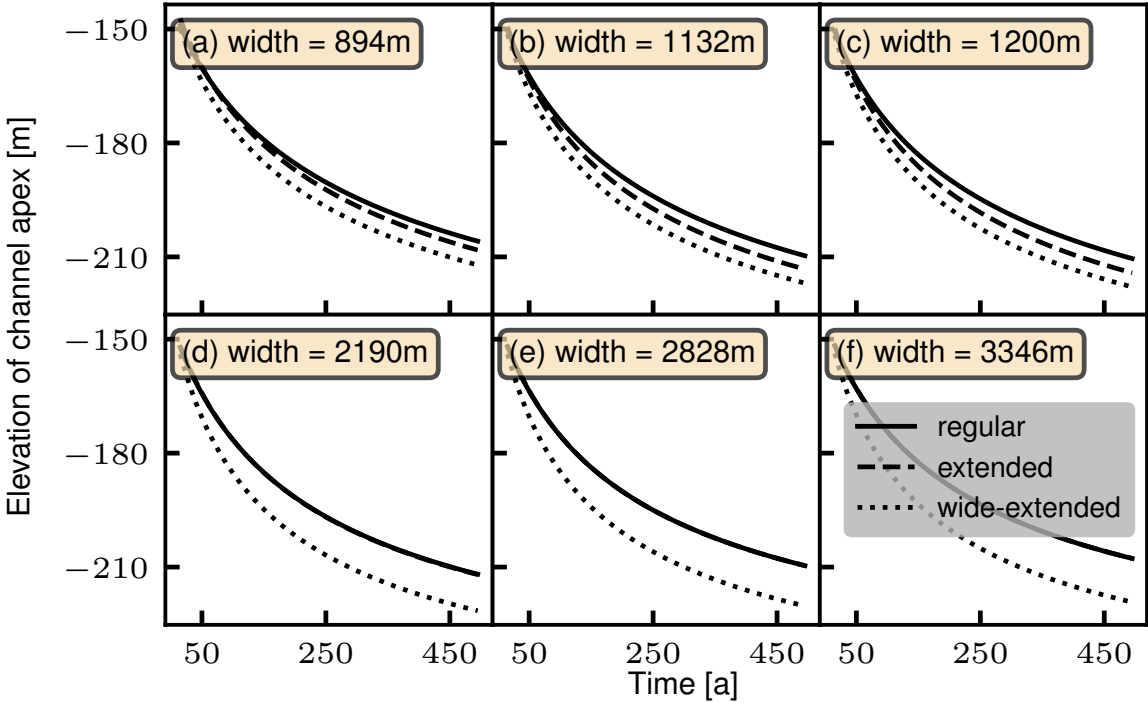


**Figure 13.:** Different channel widths for the three domain sizes (regular, extended and wide-extended). Y-axis hold the elevation of the channel amplitude. X-axis depicts the timesteps (up to 500 years). Larger domains show faster closing rates than smaller domains (regular: solid vs. wide-extended: dotted).

#### 4.2. Grounding-line sourced ice-shelf channel (3-D)

With the 3-D set-up, a different source of ice-shelf channel initiation is introduced. This stands in contrast to the 2-D set-up. As explained in chapter 3, the bedrock is lifted up to 250 m during 50 years. For simplification, the domain length is cut across the flow direction, firstly 4 km downstream of the grounding line and secondly 1 km before the outer shelf ridge (shelf front). Thus, the total plotted domain is 19 km long. Furthermore, the total width of 10 km is cut to a total width of 4 km (3 km of each side). (Figure 14). Different Gaussian perturbations are implemented at the center of the grounding-line as depicted in Table 3 for the real distances and in Figure 3 for a schematic illustration. The following figures show examples, by comprising two different runs of a narrow and wide bedrock perturbation. Figure 14 shows the cropped ice-shelf domain in the upper panel. Three cross sections are set to depict the lower sub-shelf region where the basal channel is incised.

Figure 14 describes the deviation of hydrostatic equilibrium of a cropped ice shelf area with three supplementary cross sections (red, solid lines) for  $t=200$  years and two bedrock perturbation widths. These are 200 m for the narrow and 800 m for the wide perturbation. The profile plots (A-A', B-B' and C-C') depict the HD, as well as the modelled thickness (black, solid) and calculated hydrostatic thickness (blue, dashed). The bridging pattern is shown in the sub-plots for the respective cross section. Characteristic patterns for (a) are the observed strong hydrostatic imbalances at the channel flanks. This pattern can be observed from the closest distance to grounding line up to the shelf front. In addition, these imbalances tend to decrease with increasing distance from the grounding-line, but only for increasing distance from the channel apex. This is also observed in the corresponding cross-sections, where the HD converges towards zero deviation.

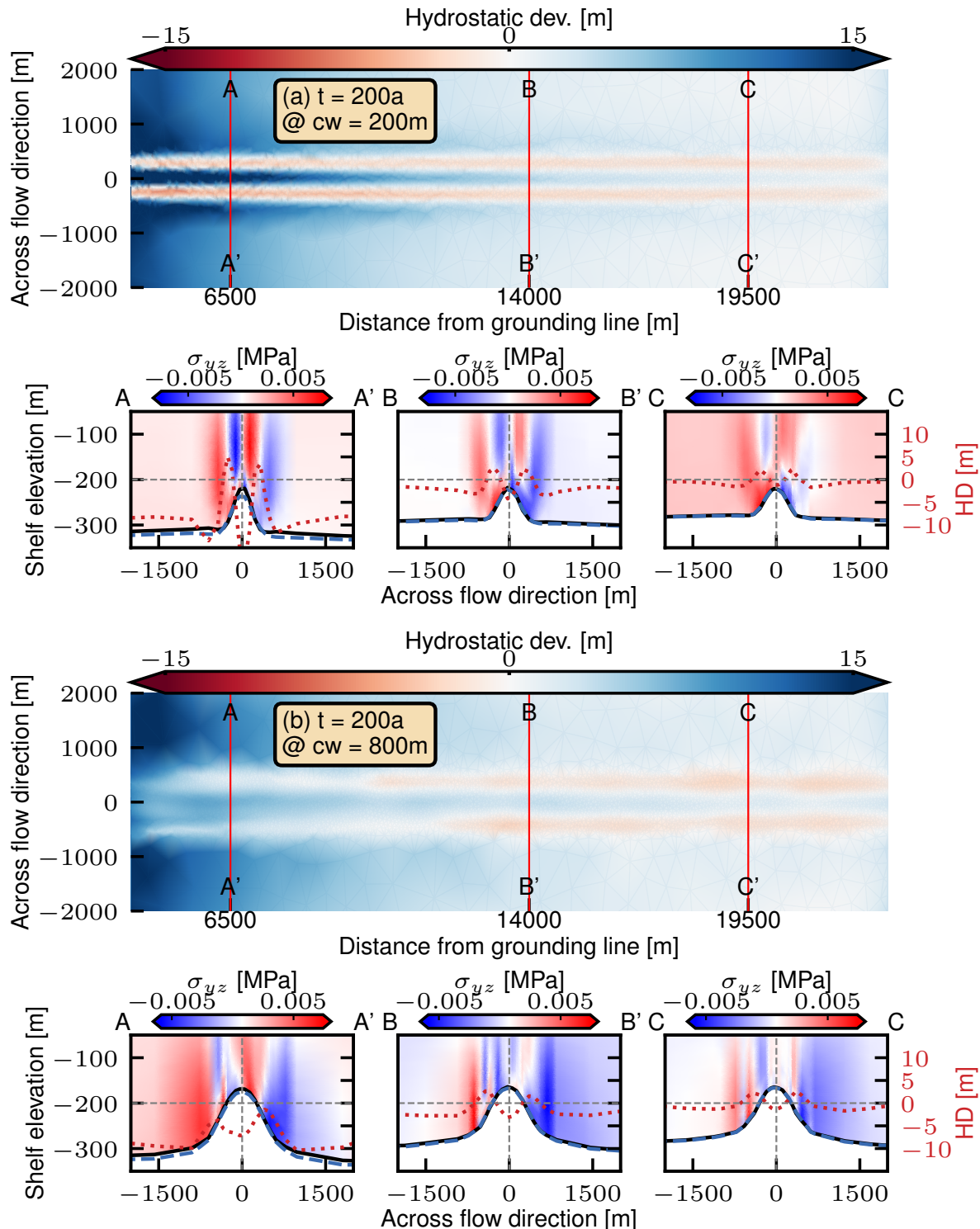


**Figure 14.**: Deviation of hydrostatic equilibrium of a cropped ice shelf area with three supplementary cross sections (red, solid lines) for  $t=200$  years and two bedrock perturbation widths; 200 m and 800 m. Profile plots ( $A-A'$ ,  $B-B'$  and  $C-C'$ ) with corresponding HD, as well as modelled thickness (black, solid) and calculated hydrostatic thickness (blue, dashed). Bridging is depicted in the sub-plots for the respective cross section. Increased hydrostatic deviation from grounding-line (left from plot boundary) to shelf front for channel flanks.

Maximum bridging values for each cross section along the flow distance are decreasing from 0.01 MPa for A-A' to C-C' with 0.006 MPa. In contrast, the channel induced from the wider bedrock perturbation (b) shows less hydrostatic deviation at the channel flanks with decreasing distance to the grounding-line. The overall pattern is less clear and seems to increase towards the shelf-front. This inconsistency is also depicted in the bridging pattern. The calculated maximum bridging values for the wide channel are for the transect A-A' 0.05 MPa (close to the grounding-line) and for C-C' 0.08 MPa (close to the shelf front). This result is inverse to the obtained maximum bridging values for the narrower channel. Here, the obtained value for the highest maximum bridging value is located at the closest cross-section to the grounding-line (C-C').

Figure 15 depicts the RMS (here, the RMS is calculated for the footprint of the corresponding model-domain, see Appendix B) of hydrostatic deviation for the y-axis and channel widths for the x-axis. The included simulations with different widths are as following: 200, 250, 300, 400, 450, 500, 550, 600, 800, 900, 950, 1000 and 1200 m. The subplots a-d show the same calculations for different time steps. The time steps are for a = 30 years, for b = 70 years, for c = 100 years and for d = 200 years.

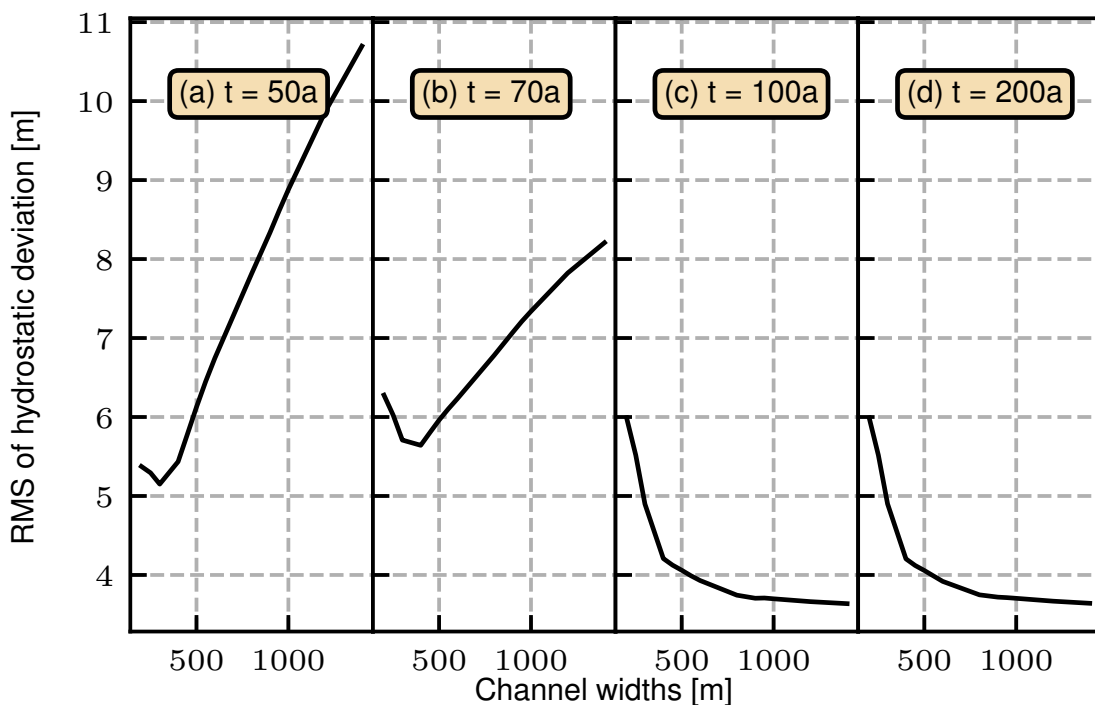


**Figure 15.:** RMS of hydrostatic deviation vs. channel widths for four different time steps: (a) = 50 years, (b) = 70 years, (c) = 100 years, (d) 200 years. (a) and (b) show a significant linear increase of the RMS of HD with increasing channel width, whereas (c) and (d) decrease exponentially.

The subplots can be subdivided in two remarkable parts. The first part includes (a) and (b) and covers the first 70 years. There, the magnitude of the RMS is strongly, linearly increasing with increasing channel widths. This is valid for channel widths approximately bigger than 500 m. Values can be as high as 7 m for the RMS calculation for channel widths bigger than 1000 m. The second part containing (c) and (d), starts at 100 years and ends after 200 years. Here, the RMS is exponentially decreasing with increasing channel widths. The RMS values start at 6 m for channel widths of 200 m and diminish to values of 3 m of channel widths of 1200 m.

## 5. Discussion

The following section starts with the discussion of the obtained model results from the internal velocity pattern. Subsequently, the hydrostatic imbalances are linked with the horizontal shear stress and are derived numerically. In section 5.3 the main subject is discussed, which treats the influence of different channel widths on the deviation of hydrostatic equilibrium. The final two sections contain the discussion among the impact of wider domain extents for the 2-D case and the 3-D bedrock channel initiation as a stand alone. The following discussion does not directly focus on comparing the 2-D and 3-D case in order to determine implications from different channel widths. Yet, it is necessary to analyse the respective impact of each scenario on the interior dynamics of an ice-shelf and refer to likely mechanisms which could lead to a possible destabilisation of an ice-shelf.

### 5.1. Interpretation of vertical/horizontal velocities and hydrostatic imbalances (2-D)

Enhanced vertical velocity  $u_y$  of the ICD and in vicinity show the general influence of the 2-D geometry set-up. Vertical velocities of the sub ice-shelf domain clearly depend on the sub-shelf geometry. Here, negative ice-flow velocities determine the inflow of the closing channel. Similar results are shown by Drews (2015) with a 3-D set-up; here in Figure 7.

For horizontal velocities  $u_x$  ice is slower between the margins of the narrower channel than for the wider channel. In general, horizontal velocities compensate for an increased strain rates in channel vicinity (strain rates not shown here) which strongly depend on the ice-softness. Thus, the magnitude of strain and horizontal velocities, might change if the softness parameter  $A$  is changed. Zero flow velocities above the channel apex highlight the flow convergence in the middle of the domain.

As proposed in Vaughan et al. (2012), the ice surface tries to compensate for the hydrostatic disequilibrium, induced by the channel geometry. This results in a longitudinal compression, whereas the shelf bottom experiences longitudinal extension, because ice seeks to compensate for surface depression in a linear-elastic behaviour. This impact of the changing surface geometry of the outer peak deviation can also be related with the vertical flow velocities of the cross section depicted in Figure 8, (b). The theory however, is also known as the conceptual model of a linear elastic thin beam (e.g. Vaughan (1995)). The influence of this flexure can be seen in e.g. Figure 5 in the OCD, named outer peak deviation. Due to compression, the ice is locally depressed in the outer margins. A more detailed discussion of this theory proceeds in section 5.3.

## 5.2. Implications of hydrostatic imbalances on horizontal shear stress

In subsection 4.1.2 two runs are chosen (which benchmark a narrow and a wide channel) with two different channel widths. They are evaluated with respect to the alternating horizontal shear stress. Studies from Drews (2015) with a 2-D and 3-D synthetic, full Stokes set-up can be proved: The sub-shelf channel width strongly correlates with the alternating bridging pattern of the ice-shelf cross-section (Figure 9). Figure 10 shows by scaling of the axis, that maxima and minima of the HD (where the absolute deviation of the hydrostatic equilibrium is highest) correspond to zero bridging stresses. Consequently, the highest bridging stresses occur where the overburden ice-column transfers these horizontal stresses to the channel flanks (Greve & Blatter 2009). This phenomenon emerges within the ICD for the channel peak deviation (position of the channel apex) and in the OCD for the outer peak deviation, whereas the latter only depicts minor effects (Figure 5). This small imbalance most likely develops due to the pseudo linear-elastic behaviour of the structured grid and the lateral hydrostatic boundary condition. When the channel itself is closing (see subsection 4.1.5) during the transient simulation and compensating for the instantaneous geometry change in the upper surface  $z_s$ , the nodes of the mesh of the channel flanks moving downwards. Eventually, due to hydrostatic force of the lateral boundary-condition, the shelf is not able to compensate for this stress and deforms the mesh to an anticline (refers to outer peak deviation). This is shown in Figure 16 and further explained in the corresponding section.

Figure 10 and subsection 4.1.2 show, that the function  $f(x)$  contains the HD as a negative (inverted derivative; in order to maintain and match the gradient of the HD derivative) derivative and vice-versa, if the derivative is calculated, HD can be integrated to obtain  $f(x)$ . The numerical approach explained in subsection 4.1.2 leads to the assumption, that this specific relationship might be solved analytically. Accordingly, by calculating the hydrostatic thickness with the freeboard height  $h_{asl}$  in Equation 2.5 and Equation 2.7, there is a potential for obtaining horizontal shear stress gradients directly from the free/top surface  $z_s$ , as surface expressions of basal shelf channels are evidenced by satellite imagery as e.g. from Le Brocq et al. (2013) or Langley et al. (2014). These surface expressions, reflect major perturbations in the bottom interface. These surface anomalies can be minor at the top surface. Deriving the bridging gradient from the top surface must consider to reinforce the signal. Figure 19 show squeezed plots of bridging-profiles. In contrast, the derivatives of  $z_s$  cannot reproduce this magnitude. This effect must be taken into account when this numerical differentiation is solved analytically. As a general effect, bridging usually prevents deriving the correct basal mass balance, as the latter depends on the original ice thickness (e.g. Rignot & Steffen (2008)). Corroborated that data acquisition from e.g. altimetry can be complicated as demonstrated by Pritchard et al. (2012) and summarized by the technical report of the Intergovernmental Panel of Climate Change (IPCC) (Science et al. 2007). The following points are a hand-full components, which contribute to a great uncertainty when calculating the surface and basal mass balance:

1. Real-world scenarios and the precise calculation of ice-shelf thickness is erroneousness
2. The correct modelling of tides, near surface-firn processes, which can enhance density anomalies and are neglected in Equation 2.7
3. In general a sea-level rise and the correct calculation of the freely floating surface of an ice-shelf, where changes in elevation may vary between 10% and 100% after Pritchard et al. (2012)

In conclusion, the derivation of the dependency between lateral shear stresses and surface expression

can minimize erroneousness in calculated ice thicknesses, as bridging stresses can derive hydrostatic imbalances.

### 5.3. Increasing channel width vs. hydrostatic imbalances (2-D and 3-D)

Despite local, small scale melt patterns, the thinning of ice shelves is generally well studied. Thus, locally distributed sub-shelf channels may be of greater importance referring to the mechanical disintegration of ice shelves than expected (Drews 2015; Marsh et al. 2016; Millgate et al. 2013; Stanton et al. 2013). Predominantly in subsection 4.1.4, the dependency of increasing channel width on the channel peak deviation as well as the RMS of the HD is analysed.

In the following, the relationship between the deviation of hydrostatic equilibrium and the channel width is described. The most profound result reveals a non-linear relationship between the channel width and the HD, not only for the channel peak in the ICD, but also for the whole shelf domain (Figure 12). Slower relaxation to hydrostatic equilibrium can be expected where the slope is steep, whereas a flat slope indicates a faster relaxation of the ice-shelf towards hydrostatic equilibrium. This infers that there must be a crucial tipping point, which can roughly be estimated between a channel width of 600 m and 1000 m for 2-D model results. Grounding-line sourced channels show the same exponential dependency of channel width on HD as 2-D instantaneous implemented channels. This exponential dependency might be explained by the scheme depicted in Figure 16.

(a) undeformed ice shelf with channel at t=0 a



(b) deformed ice shelf during simulation

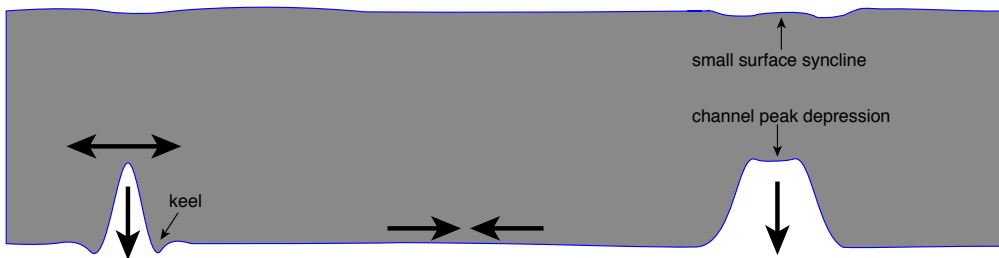


**Figure 16.:** The general hypothesis of deformation pattern for a 2-D model case. (a) describes two different channel widths (narrow channel on the left side, wide channel on the right side for a critical width) before simulation. (b) shows assumed flexing pattern of channel. Arrows show the direction of flexing response. The critical width shows the result of a pseudo linear-elastic deformation of 2-D model set-up. The critical channel width develops a depression at the channel apex, with minor adjustments at the surface.

The pseudo linear-elastic behaviour of this model, already described in section 5.1 counteracts the decay of a sub-shelf channel when a bridging threshold is passed. This means in general, that this effect is accompanied by relatively high bridging values. Yet, this specific bridging threshold is unknown, and may depend on different factors, such as domain size or in general the consideration of the ice-rheology. The model-setting does not account for viscoelasticity. In general, ice behaves due to its polycrystalline structure as a viscoelastic material (Gudmundsson 2011) and not solely viscous. This might be important on shorter, transient time-scales. Especially for the conducted model-runs it might be important because short-term forcings, such as the instantaneous implemented channels, have a waste impact on long-term behaviour of an ice-shelf. This effect is validated by MacAyeal et al. (2015).

However, this results in a downward bending of the channel keel (Figure 16) for narrow channels (also affects the outer peak deviation due to compression) and a slower decay of the whole instantaneous channel geometry. The channel shape of the channel apex is maintained. In contrast, at a given critical width, which is most likely also linked to a certain slope at the channel flank, the channel keels are not present. Therefore, only the channel apex experiences depression and thus influences the channel peak deviation. Eventually, the difference between the modelled ice thickness and the calculated hydrostatic thickness is exponentially lower and describes the non-linear behaviour of these increasing channel widths on the HD. By contrast, linearity is then obtained for very narrow, imbalanced and very wide, equilibrated channels with a plateau. These plateau shaped channels are predominant for channel-widths bigger than approximately 1000 m. The described model results however, do not show major surface reflections of the sub-shelf perturbations. The signal of these perturbations might get lost and is thus only moderately recognisable at the top surface  $z_s$ .

If these findings are put into a broader context, the question arises, whether the increasing channel width decreases the ability of the ice-shelf to buttress inland ice-flow or vice-versa. Millgate et al. (2013) show with a general circulation model, that simulation results with increasing narrow channels in the sub shelf regime tend to diminish the mean basal melt rate, because the product of frictional velocity and thermally driving is positively correlated with the melt rate (eg. Holland et al. (2008b) and Holland & Jenkins (1999)). Thus regions of narrower channels are less vulnerable as melting is more evenly distributed over the whole sub-shelf domain. This result may confirm the theory, that narrow channels can stabilize the ice-shelf and underpins our results that a certain critical width (see Figure 16) of the ice-shelf channels may contribute with a significant order to the determination, whether local melting is intensified.

The analysis of this relationship should be once more conducted by a more distinct model, which conflates ice/ocean interactions with full dynamics of an ice-sheet/shelf, as any oceanic changes in salinity, temperature and thus thermally layered regimes are neglected. Furthermore, the general height to width ratio of channels is not analysed, as this thesis only treats varying widths with a constant height. This ratio might also be of importance, when determining the critical width explained above in Figure 16. Addressing these interactions seems crucial, as e.g. West Antarctica currently experiences thinning, which is mainly caused by sub-ice-shelf melting through CDW (e.g. Jacobs et al. (2011), Dutrieux et al. (2014a) and Jenkins et al. (2018)).

#### **5.4. Larger shelf domains amplify channel closing (2-D)**

Following section 5.3, if results of e.g. Millgate et al. (2013) or V. Gladish et al. (2012) are proven to be correct, that narrower channel might yield to a strengthen of an ice-shelf, then the findings unrolled in the results in section 5.3 can amplify this process as follows: the boundary condition for the lateral side walls of the ice-shelf is the product of the hydrostatic pressure  $p$  and the gravitational acceleration  $g$ , which can be described as the hydrostatic force balance. This pressure forcing increases with an increase of the domain (for 2-D in x-direction) and results not only in a faster decrease of the channel apex for larger domains, but also in a faster decrease with increasing channel width's. This effect is depicted in Figure 13 for e.g. CH\_894\_2D and CH\_2192\_2D including runs with a wide-extended domain. These faster closing rates for larger domains might higher horizontal flow velocities. As a result, channels close faster for larger domains and wider channels (see horizontal flow velocities in Figure 6). Apparently, the difference for closing rates within narrower channels is noticeably lower (Figure 13). In general, this effect may lead to a stronger depression of the channel apex, as described in the former section. In general, model results are clearly dependent on changing domain sizes. This should be considered in other models, when the magnitude of absolute values is compared.

#### **5.5. Induced sub-shelf channel advection with bedrock perturbations (3-D)**

The following section will treat first and foremost the 3-D model results and where the differentiation of the origin and evolution of basal ice-shelf channels is crucial. Alley et al. (2016) show that grounding-line sourced channels may form due to lack of interactions with warm water, due to their shallow ice draft, whereas ocean-sourced channel often originate where warm circumpolar deep waters (CDW) can better interact with the bottom of an ice-shelf. Newer findings from Drews et al. (2017) reveal with Airborne- and ground-based radar, that Eskers, deposited as sedimentary perturbations at the grounding-line, can shape the geometry of basal ice-shelf channels which propagate towards the shelf front. Furthermore, Drews et al. (2017) show, that surface channels can partly exhibit relict ridges in the main channel depression as shown in Figure 16.

The results of the 3-D model indicate, that grounding-line sourced channels, which advect passively through the ice-shelf, maintain their imbalances at the channel flanks, where bridging stresses are the highest. The high linear increasing deviation during the first 70 years depicted in Figure 15 is interpreted as an intensified signal of the time dependent growth of the bedrock bump at the grounding line. Interestingly is the fast inversion of this signal between 70 and 100 years. Imbalances transferred from the grounding line are thus significantly higher during the bedrock growth than after. The imbalances and bridging patterns close to the grounding line are longer sustained for narrower channels than for wider channels. This coincides with the maximum bridging values obtained from the simulation of a narrow and a wide channel and confirms the results of the simpler 2-D model, where bridging increases with decreasing channel-width. Furthermore, it seems that wider channels experience faster relaxation and less bridging towards the grounding line. This might infer a relationship between upstream channel formation at the grounding-line and downstream relaxation. If sedimentary processes or hydrological conduits mitigate, the bedrock might not further drastically change its shape. As a result, depending on the spatial extent (width) of sedimentation process at the grounding-line, wider channels might decay faster than narrower channels in closer vicinity

of the ice-shelf. Thus, as wider channels decay faster, channels may indicate surface relict ridges. These relict ridges have been observed by Drews (2015). This is however strongly dependent on the channel size and width, and cannot be reproduced, yet. Furthermore, the geometry of ice-shelf channels is influenced by numerous mechanisms, which may enhance with increasing distance from the grounding line. However, a benefit from this hypothesis can be e.g. the derivation of elder grounding-line sourced sedimentation or hydrological conduit processes.

Dutrieux et al. (2014b) show in their study, that the specific geometry of channels is of major importance, as the flanks are usually not flat (slope 3-5°) and the channel peaks often show terrace alike shapes. The channel drafts do not provide these terraces, as they are initialized through a Gaussian-bell function. This however indicates, that the difference in slope steepness is a function of the given channel width with steeper channel flanks for narrow channels and vice-versa. In a broader sense: multiple studies already explained the correlation of modified ocean circulation at a local scale of ice-shelf channels (e.g. V. Gladish et al. (2012), Rignot & Steffen (2008) or Stanton et al. (2013)). Rising, buoyant water plumes gain, due to their increasing velocity, more heat from deeper water levels (Holland et al. 2008a; Jenkins & Doake 1991). Hence, steep slopes may favour melting at steep channel flanks (Dutrieux et al. 2014b), enhancing a positive feedback within the velocity of the plume, steep channel flanks and melt rates (Sergienko 2013). Thereby, a link to the results can be drawn where areas with highest bridging stresses might favour high melt rates (e.g. Figure 9 and Figure 10).

## 5.6. Remarks and model limitations

Uncertainties of model predictions of real-world scenarios in the ice sheet/ shelf modelling community are high. There are major challenges, as e.g.:

- i) the coupling of ice dynamics of ice sheet and shelf flow regimes, referring to the grounding-line (or zone) as one of the most important features and transition zone
- ii) resolving ice/ bed interface not only for ice sheets slow creep motion, but also for ice shelves, which are in contact with locally grounded features called ice rises and ripples (Matsuoka et al. 2015)
- iii) thermodynamics and the corresponding continua as e.g. water for ice/ocean interfaces, considering tides, salinity etc. or in hydrological surface or bed processes which can also comprise sedimentation processes at the ice/ bed interface.

The synergy and the advancing comprehension for these complicated physical processes is a major task. In addition, the computational effort might be a constraint for future work. Hence, the idealized 2-D and 3-D models in this thesis are neither supposed to include all these processes, nor to disregard them, when putting them into context. In general, we conduct the model runs in order to obtain sensitive data to changing geometries at the sub-shelf interface. However, the outreach of purely synthetic models is limited. A general parametrization is crucial and must be constrained by real data. For the 3-D case, the conducted model runs do not account for basal melt parametrization, but only for sea-pressure. This scenario however, might not be realistic as oceanic melting is the main driver of the current mass loss of most of the Antarctic ice/sheet shelf (Dutrieux et al. 2014b; Jacobs et al. 2011; Jenkins et al. 2018). In general, melting parametrisation is unrealistic, as they usually over- or underestimate melting (Favier

et al. 2019). In a broader sense, the prescribed parameters in Table 1 are very sensitive to adjustments and can result e.g. in a change of a significant magnitude, thus it is difficult to quantitatively compare results with other authors. For example: the change of the exponent  $n$ , which is usually equal to 3 (verified in laboratory by Budd & Jenssen (1989)) used in the non-linear ice-rheology for ice flow of Glen's flow law, will quantitatively influence the results. From a qualitative perspective however, the change may be negligible. Further limitation for the 3-D case might be, that the grounding-line is fixed and not able to retreat. However, the grounding-line defines the transition between ice-sheet and ice-shelf, where the ice-flux is foremost an increasing function of ice-thickness. A retreat of the grounding-line on a retrograde bed-slope might implicate higher resulting fluxes and finally an impact on the flow pattern of an ice-shelf, which is not considered in the set-ups. However, as this thesis shows, modelling approaches with synthetic set-ups can help to better understand the influence of changing parameters on ice-dynamics. Modelling approaches with real-world geometries might not be able to reproduce clear separations of important processes in these ice-dynamics.

## 6. Conclusion

A full-Stokes, finite-element model is used to model transient ice-shelf channel evolution with a synthetic and idealized geometry in 2-D and 3-D. The 2-D set-up includes an instantaneous channel implementation of a transect of an ice-shelf. The 3-D set-up uses a transient bedrock perturbation at the grounding-line to initiate a sub ice-shelf channel advection. Both set-ups focus on the correlation between alternating channel widths and the deviation of hydrostatic equilibrium. In addition, internal dynamics of velocities and predominantly horizontal shear stresses are investigated.

The main conclusions are the following:

- This first negative derivative of the gradient of horizontal shear stress as a lateral profile of an ice-shelf transect is the gradient of the deviation of hydrostatic equilibrium. Derivatives of the top surface  $z_s$  are approximately the gradient of the horizontal shear stress as a first derivative and the deviation of hydrostatic equilibrium as a second derivative. In general, the top surface  $z_s$  reflects a weakened signal of the bottom surface  $z_b$ .
- The deviation of hydrostatic equilibrium is an exponentially decreasing function of the channel width. At a certain channel width, the channel apex deforms due to the decrease of horizontal shear stresses and experiences depression.
- Increasing domain sizes of ice-shelves amplify channel closing. Wider channels close faster than narrower channels.
- By implementing a bedrock perturbation at the grounding-line (transient uplift of bedrock), a first 3-D full-Stokes modelling set-up can successfully create channel formation advecting downstream to the shelf-front.

Predicting future ice-sheet mass balance strictly depends on the understanding of a sum of physical key processes of ice-ocean interaction, as well as atmospheric forcing and how they are implemented within model set-ups. In this context, the ice-shelf channel's width can play a crucial role, as the changing channel width influences the stress regime in its vicinity and thus represents a critical location for the ice-ocean interface. However, the performed analysis of a synthetic set-up neglects atmospheric or ocean driven processes. These should be taken into account when approaching future projects and research of a similar fashion. The internal shear-stress gradients and hydrostatic imbalances can be directly linked to surface anomalies. This relationship is qualitatively analysed and numerically validated. However, this thesis encourages to analytically solve the relationship of top-surface geometry and internal ice dynamics, as some key-aspects (e.g. the order of magnitude) of this relationship are not solved yet.

## Bibliography

- Alley, K. E., Scambos, T. A., Siegfried, M. R. & Fricker, H. A. (2016): Impacts of Warm Water on Antarctic Ice Shelf Stability through Basal Channel Formation. *Nature Geoscience* 9(4), 290–293.
- Angelis, H. D. & Skvarca, P. (2003): Glacier Surge After Ice Shelf Collapse. *Science* 299(5612), 1560–1562.
- Berger, S., Favier, L., Drews, R., Derwael, J.-J. & Pattyn, F. (2016): The Control of an Uncharted Pinning Point on the Flow of an Antarctic Ice Shelf. *Journal of Glaciology* 62(231), 37–45.
- Bindschadler, R. (2006): Hitting the Ice Sheets Where It Hurts. *Science* 311(5768), 1720–1721.
- Budd, W. F. & Jenssen, D. (1989): The Dynamics of the Antarctic Ice Sheet. *Annals of Glaciology* 12, 16–22.
- Depoorter, M. A., Bamber, J. L., Griggs, J. A., Lenaerts, J. T. M., Ligtenberg, S. R. M., van den Broeke, M. R. & Moholdt, G. (2013): Calving Fluxes and Basal Melt Rates of Antarctic Ice Shelves. *Nature* 502(7469), 89–92.
- Dias dos Santos, T., Morlighem, M., Seroussi, H., Devloo, P. & Simoes, J. (2018): Implementation and Performance of Adaptive Mesh Refinement in the Ice Sheet System Model (ISSM v4.14). *Geoscientific Model Development Discussions* 1–32.
- Drews, R. (2015): Evolution of Ice-Shelf Channels in Antarctic Ice Shelves. *The Cryosphere* 9(3), 1169–1181.
- Drews, R., Pattyn, F., Hewitt, I. J., Ng, F. S. L., Berger, S., Matsuoka, K., Helm, V., Bergeot, N., Favier, L. & Neckel, N. (2017): Actively Evolving Subglacial Conduits and Eskers Initiate Ice Shelf Channels at an Antarctic Grounding Line. *Nature Communications* 8, 15228.
- Durand, G., Gagliardini, O., de Fleurian, B., Zwinger, T. & Meur, E. L. (2009): Marine Ice Sheet Dynamics: Hysteresis and Neutral Equilibrium. *Journal of Geophysical Research: Earth Surface* 114(F3).
- Dutrieux, P., Rydt, J. D., Jenkins, A., Holland, P. R., Ha, H. K., Lee, S. H., Steig, E. J., Ding, Q., Abrahamsen, E. P. & Schröder, M. (2014a): Strong Sensitivity of Pine Island Ice-Shelf Melting to Climatic Variability. *Science* 343(6167), 174–178.
- Dutrieux, P., Stewart, C., Jenkins, A., Nicholls, K. W., Corr, H. F. J., Rignot, E. & Steffen, K. (2014b): Basal Terraces on Melting Ice Shelves. *Geophysical Research Letters* 41(15), 5506–5513.
- Dutrieux, P., Vaughan, D. G., Corr, H. F. J., Jenkins, A., Holland, P. R., Joughin, I. & Fleming, A. H. (2013): Pine Island Glacier Ice Shelf Melt Distributed at Kilometre Scales. *The Cryosphere* 7, 1543–1555.
- Favier, L., Jourdain, N. C., Jenkins, A., Merino, N., Durand, G., Gagliardini, O., Gillet-Chaulet, F. & Mathiot, P. (2019): Assessment of Sub-Shelf Melting Parameterisations Using the Ocean–Ice-Sheet Coupled Model NEMO(v3.6)–Elmer/Ice(v8.3). *Geoscientific Model Development* 12, 2255–2283.
- Fürst, J. J., Durand, G., Gillet-Chaulet, F., Tavard, L., Rankl, M., Braun, M. & Gagliardini, O. (2016): The Safety Band of Antarctic Ice Shelves. *Nature Climate Change* 6(5), 479–482.



- T. A., Payne, A. J., Rippin, D. M. & Siegert, M. J. (2013): Evidence from Ice Shelves for Channelized Meltwater Flow beneath the Antarctic Ice Sheet. *Nature Geoscience* 6(11), 945–948.
- MacAyeal, D. R., Sergienko, O. V. & Banwell, A. F. (2015): A Model of Viscoelastic Ice-Shelf Flexure. *Journal of Glaciology* 61(228), 635–645.
- Mack, S. L., Dinniman, M. S., Klinck, J. M., McGillicuddy, D. J. & Padman, L. (2019): Modeling Ocean Eddies on Antarctica's Cold Water Continental Shelves and Their Effects on Ice Shelf Basal Melting. *Journal of Geophysical Research: Oceans* 124(7), 5067–5084.
- Marsh, O. J., Fricker, H. A., Siegfried, M. R., Christianson, K., Nicholls, K. W., Corr, H. F. J. & Catania, G. (2016): High Basal Melting Forming a Channel at the Grounding Line of Ross Ice Shelf, Antarctica. *Geophysical Research Letters* 43(1), 250–255.
- Matsuoka, K., Hindmarsh, R. C. A., Moholdt, G., Bentley, M. J., Pritchard, H. D., Brown, J., Conway, H., Drews, R., Durand, G., Goldberg, D., Hattermann, T., Kingslake, J., Lenaerts, J. T. M., Martín, C., Mulvaney, R., Nicholls, K. W., Pattyn, F., Ross, N., Scambos, T. & Whitehouse, P. L. (2015): Antarctic Ice Rises and Ripples: Their Properties and Significance for Ice-Sheet Dynamics and Evolution. *Earth-Science Reviews* 150, 724–745.
- Mercer, J. H. (1978): West Antarctic Ice Sheet and CO<sub>2</sub> Greenhouse Effect: A Threat of Disaster. *Nature* 271(5643), 321–325.
- Millgate, T., Holland, P. R., Jenkins, A. & Johnson, H. L. (2013): The Effect of Basal Channels on Oceanic Ice-Shelf Melting. *Journal of Geophysical Research (Oceans)* 118, 6951–6964.
- Paolo, F. S., Fricker, H. A. & Padman, L. (2015): Volume Loss from Antarctic Ice Shelves Is Accelerating. *Science* 348(6232), 327–331.
- Pattyn, F., Schoof, C., Perichon, L., Hindmarsh, R. C. A., Bueler, E., de Fleurian, B., Durand, G., Gagliardini, O., Gladstone, R., Goldberg, D., Gudmundsson, G. H., Huybrechts, P., Lee, V., Nick, F. M., Payne, A. J., Pollard, D., Rybak, O., Saito, F. & Vieli, A. (2012): Results of the Marine Ice Sheet Model Intercomparison Project, MISMIP. *The Cryosphere* 6, 573–588.
- Pritchard, H., Ligtenberg, S., Fricker, H., Vaughan, D., Van den Broeke, M. & Padman, L. (2012): Antarctic Ice-Sheet Loss Driven by Basal Melting of Ice Shelves. *Nature* 484, 502–5.
- Rignot, E. & Steffen, K. (2008): Channelized Bottom Melting and Stability of Floating Ice Shelves. *Geophysical Research Letters* 35(2).
- Rignot, E., Velicogna, I., van den Broeke, M. R., Monaghan, A. & Lenaerts, J. T. M. (2011): Acceleration of the Contribution of the Greenland and Antarctic Ice Sheets to Sea Level Rise. *Geophysical Research Letters* 38(5).
- Rignot, E. J. M., Jacobs, S. S., Mouginot, J. & Scheuchl, B. (2013): Ice-Shelf Melting around Antarctica. *Science* 341(6143), 266–270.
- Rott, H., Rack, W., Skvarca, P. & Angelis, H. D. (2002): Northern Larsen Ice Shelf, Antarctica: Further Retreat after Collapse. *Annals of Glaciology* 34, 277–282.
- Science, I. P. o. C. C. W. G. ., Change, I. P. o. C. & I. I. P. o. C. C. W. G. (2007): *Climate Change 2007 - The Physical Science Basis: Working Group I Contribution to the Fourth Assessment Report of the IPCC*. Cambridge University Press.

Sergienko, O. V. (2013): Basal Channels on Ice Shelves. *Journal of Geophysical Research: Earth Surface* 118(3), 1342–1355.

Shepherd, A., Ivins, E. R., A, G., Barletta, V. R., Bentley, M. J., Bettadpur, S., Briggs, K. H., Bromwich, D. H., Forsberg, R., Galin, N., Horwath, M., Jacobs, S., Joughin, I., King, M. A., Lenaerts, J. T. M., Li, J., Ligtenberg, S. R. M., Luckman, A., Luthcke, S. B., McMillan, M., Meister, R., Milne, G., Mouginot, J., Muir, A., Nicolas, J. P., Paden, J., Payne, A. J., Pritchard, H., Rignot, E., Rott, H., Sørensen, L. S., Scambos, T. A., Scheuchl, B., Schrama, E. J. O., Smith, B., Sundal, A. V., van Angelen, J. H., van de Berg, W. J., van den Broeke, M. R., Vaughan, D. G., Velicogna, I., Wahr, J., Whitehouse, P. L., Wingham, D. J., Yi, D., Young, D. & Zwally, H. J. (2012): A Reconciled Estimate of Ice-Sheet Mass Balance. *Science* 338(6111), 1183–1189.

Stanton, T. P., Shaw, W. J., Truffer, M., Corr, H. F. J., Peters, L. E., Riverman, K. L., Bindschadler, R., Holland, D. M. & Anandakrishnan, S. (2013): Channelized Ice Melting in the Ocean Boundary Layer Beneath Pine Island Glacier, Antarctica. *Science* 341(6151), 1236–1239.

Thomas, R. H. (1973): The Creep of Ice Shelves: Interpretation of Observed Behaviour. *Journal of Glaciology* 12(64), 55–70.

V. Gladish, C., Holland, D., R. Holland, P. & Price, S. (2012): Ice-Shelf Basal Channels in a Coupled Ice/Ocean Model. *Journal of Glaciology* 58, 1227–1244.

van der Veen, C. J. (2013): *Fundamentals of Glacier Dynamics*. CRC Press.

Vaughan, D. G. (1995): Tidal Flexure at Ice Shelf Margins. *Journal of Geophysical Research: Solid Earth* 100(B4), 6213–6224.

Vaughan, D. G., Corr, H. F. J., Bindschadler, R. A., Dutrieux, P., Gudmundsson, G. H., Jenkins, A., Newman, T., Vornberger, P. & Wingham, D. J. (2012): Subglacial Melt Channels and Fracture in the Floating Part of Pine Island Glacier, Antarctica. *Journal of Geophysical Research: Earth Surface* 117(F3).

Wouters, B., Martin-Español, A., Helm, V., Flament, T., van Wessem, J. M., Ligtenberg, S. R. M., van den Broeke, M. R. & Bamber, J. L. (2015): Dynamic Thinning of Glaciers on the Southern Antarctic Peninsula. *Science* 348(6237), 899–903.

# **Appendices**

## A. Code and data availability

The used and created data is available on the Server of the Earth System Dynamics Research Group Tübingen and can be found here: /esd01/docs/jloos/

Data from the 3-D model:

/esd01/docs/jloos/data\_small/runs\_elmerice\_3d

Data from the 2-D model:

/esd01/docs/jloos/data\_small/runs\_elmerice\_2d

Code, figures and plots can be found in sub-folders of:

/esd01/docs/jloos/thesis

A documentation list of figures and further explanation considering the scripts can be found in the readme file:

/esd01/docs/jloos/thesis/README\_thesis.md

## B. Additional equations

### Root mean square

In order to find a significant mean value of the deviation of the hydrostatic equilibrium over the whole domain (for regular, extended and wide-extended domain), the root mean square (RMS) of each run (CH\_\*\_2D) is calculated as following:

$$RMS = \sqrt{\frac{1}{x_{dom2} - x_{dom1}} \int_{x_{dom1}}^{x_{dom2}} g(x)^2 dx}, \quad (B.1)$$

As the HD can be both, negative and positive, the mean is squared. However, the domain extents are not of equal size (see subsection 3.1.1). Hence, to ensure that the RMS-values can be compared, the considered range of mean values ( $g(x)$ ) is integrated from  $x_{dom2}$  to  $x_{dom1}$  (Table 4).

### Numerical differntiation with gaussian kernel function

The calculation of the derivative  $f'(x)$  ( $\frac{d}{dx} f(x)$ ) of a given function  $f(x)$  is done by a convolution of a derivative of a gaussian kernel. Thus, the data is smoothed by choosing a value for  $\sigma$  (small=less smoothed). The function for the gaussian kernel used is available in the scipy package of Python and is used within a simple finite difference formula as follows:

$$f'(x) = \overbrace{\frac{f(x_0) - f(x_1)}{dx}}^{\text{smoothed}}. \quad (B.2)$$

Here  $dx$  denotes the difference of the given distance  $x_0$  and  $x_1$  across flow directions. Distance values are regularly spaced.

## C. Additional figures and tables

**Table 4.: A complete summary of the 2-D model set-up, with the first set of model-runs.** The table depicts the name of the model-run, the width used within Elmer/Ice ( $w_{mod}$ ), the translated width ( $w_{real}$ ), which is the real meter scale, the size of the domain ( $x_{dom}$  and  $y_{dom}$  extent). The vertical extent  $y_{dom}$  is calculated with  $\rho_i$  and  $\rho_w$  from 2.5. Note: \*\* run executed for extended and wide-extended domain; \* runs executed solely for wide-extended domain.

Name	Channel dim. ( $w_{mod}, w_{real}$ )	Domain dim. ( $x_{dom}, y_{dom}$ )	Timespan	Cells ( $x, y$ )
CH63_2D	1000, 126 m	20 km x 0.304 km	1000 a	333x15
CH89_2D	2000, 178 m	20 km x 0.304 km	1000 a	333x15
CH110_2D	3000, 220 m	20 km x 0.304 km	1000 a	333x15
CH126_2D	4000, 252 m	20 km x 0.304 km	1000 a	333x15
CH141_2D	5000, 282 m	20 km x 0.304 km	1000 a	333x15
CH155_2D	6000, 310 m	20 km x 0.304 km	1000 a	333x15
CH167_2D	7000, 334 m	20 km x 0.304 km	1000 a	333x15
CH179_2D	8000, 358 m	20 km x 0.304 km	1000 a	333x15
CH190_2D	9000, 380 m	20 km x 0.304 km	1000 a	333x15
CH400_2D**	10000, 400 m	20 km x 0.304 km	1000 a	333x15
CH566_2D**	20000, 566 m	20 km x 0.304 km	1000 a	333x15
CH692_2D**	30000, 692 m	20 km x 0.304 km	1000 a	333x15
CH800_2D**	40000, 800 m	20 km x 0.304 km	1000 a	333x15
CH894_2D**	50000, 894 m	20 km x 0.304 km	1000 a	333x15
CH980_2D**	60000, 980 m	20 km x 0.304 km	1000 a	333x15
CH1058_2D**	70000, 1058 m	20 km x 0.304 km	1000 a	333x15
CH1132_2D**	80000, 1132 m	20 km x 0.304 km	1000 a	333x15
CH1200_2D**	90000, 1200 m	20 km x 0.304 km	1000 a	333x15
CH1264_2D*	100000, 1264 m	20 km x 0.304 km	1000 a	333x15
CH1788_2D*	200000, 1788 m	20 km x 0.304 km	1000 a	333x15
CH2190_2D*	300000, 2190 m	20 km x 0.304 km	1000 a	333x15
CH2530_2D*	400000, 2530 m	20 km x 0.304 km	1000 a	333x15
CH2828_2D*	500000, 2828 m	20 km x 0.304 km	1000 a	333x15
CH3098_2D*	600000, 3098 m	20 km x 0.304 km	1000 a	333x15
CH3346_2D*	700000, 3346 m	20 km x 0.304 km	1000 a	333x15
CH3578_2D*	800000, 3578 m	20 km x 0.304 km	1000 a	333x15
CH3794_2D*	900000, 3794 m	20 km x 0.304 km	1000 a	333x15

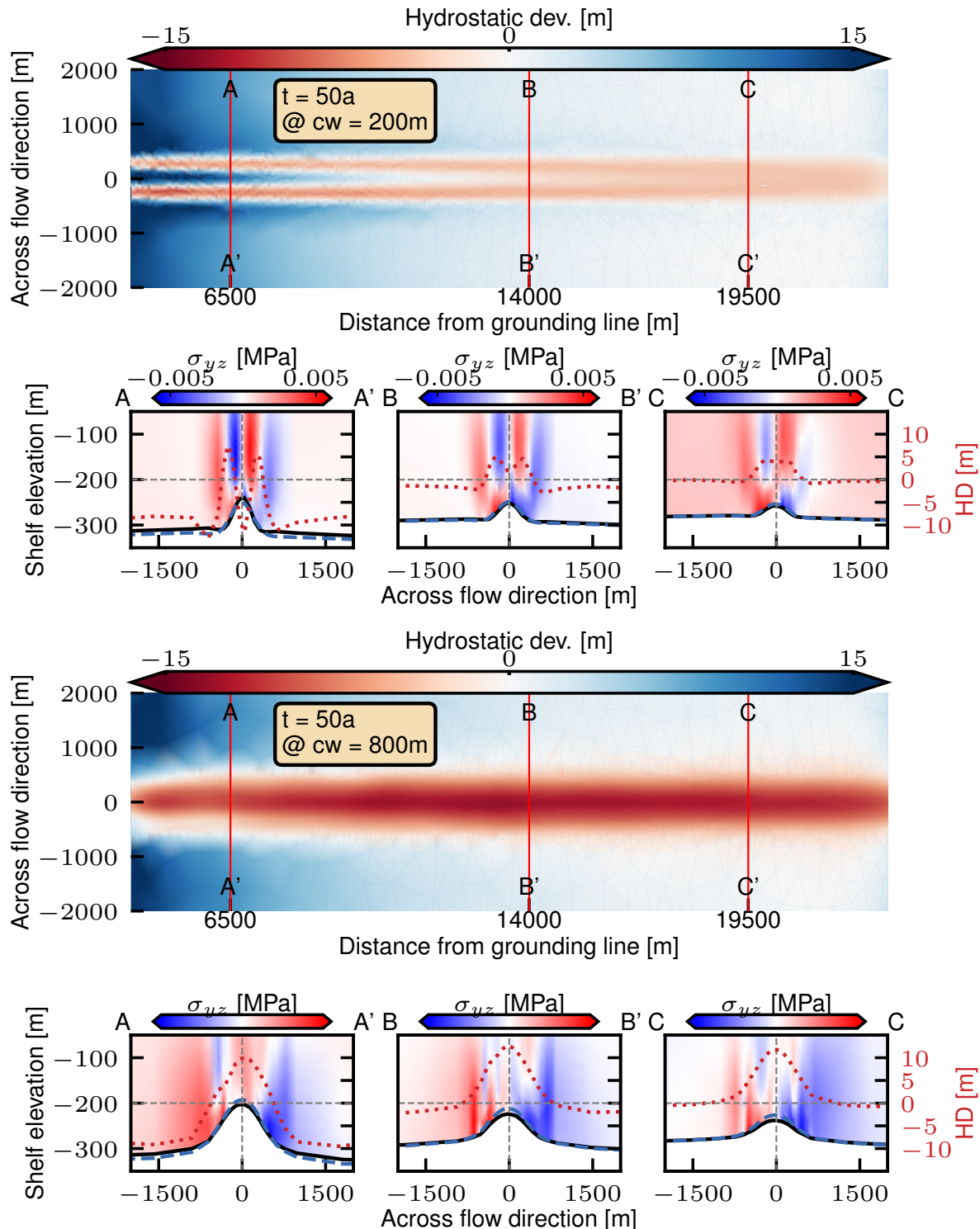


**Figure 17.:** Deviation of hydrostatic equilibrium of a cropped ice shelf area with three supplementary cross sections (red, solid lines) for  $t=50$  years and two bedrock perturbation widths; 200 m and 800 m. Profile plots ( $A-A'$ ,  $B-B'$  and  $C-C'$ ) with corresponding HD, as well as modelled thickness (black, solid) and calculated hydrostatic thickness (blue, dashed). Bridging is depicted in the sub-plots for the respective cross section. Increased hydrostatic deviation from grounding-line (left from plot boundary) to shelf front for channel flanks.

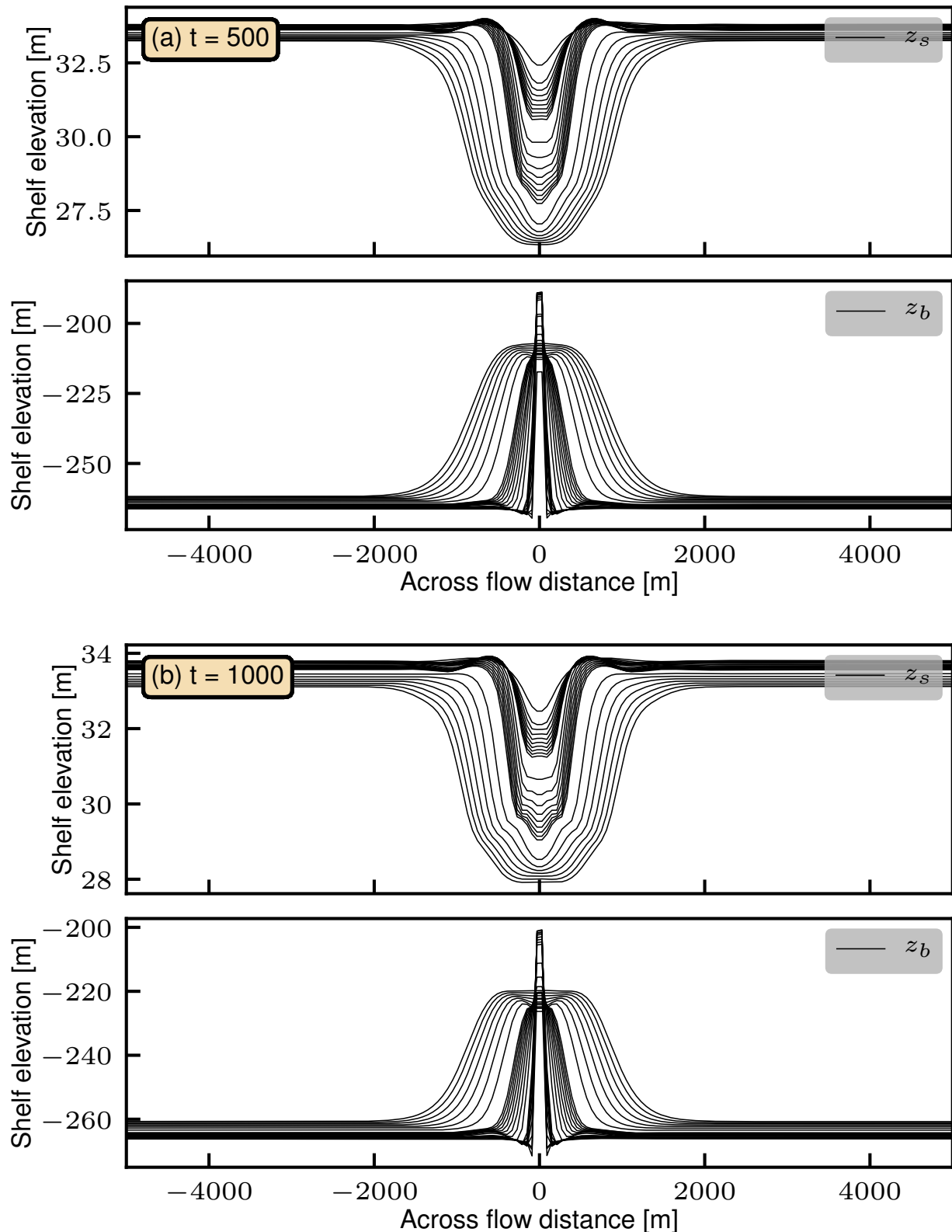


**Figure 18.: (a)** shows top surface  $z_s$  and bottom surface  $z_b$  of all model-runs after 500 years. **(b)** shows top surface  $z_s$  and bottom surface  $z_b$  of all model-runs after 1000 years.

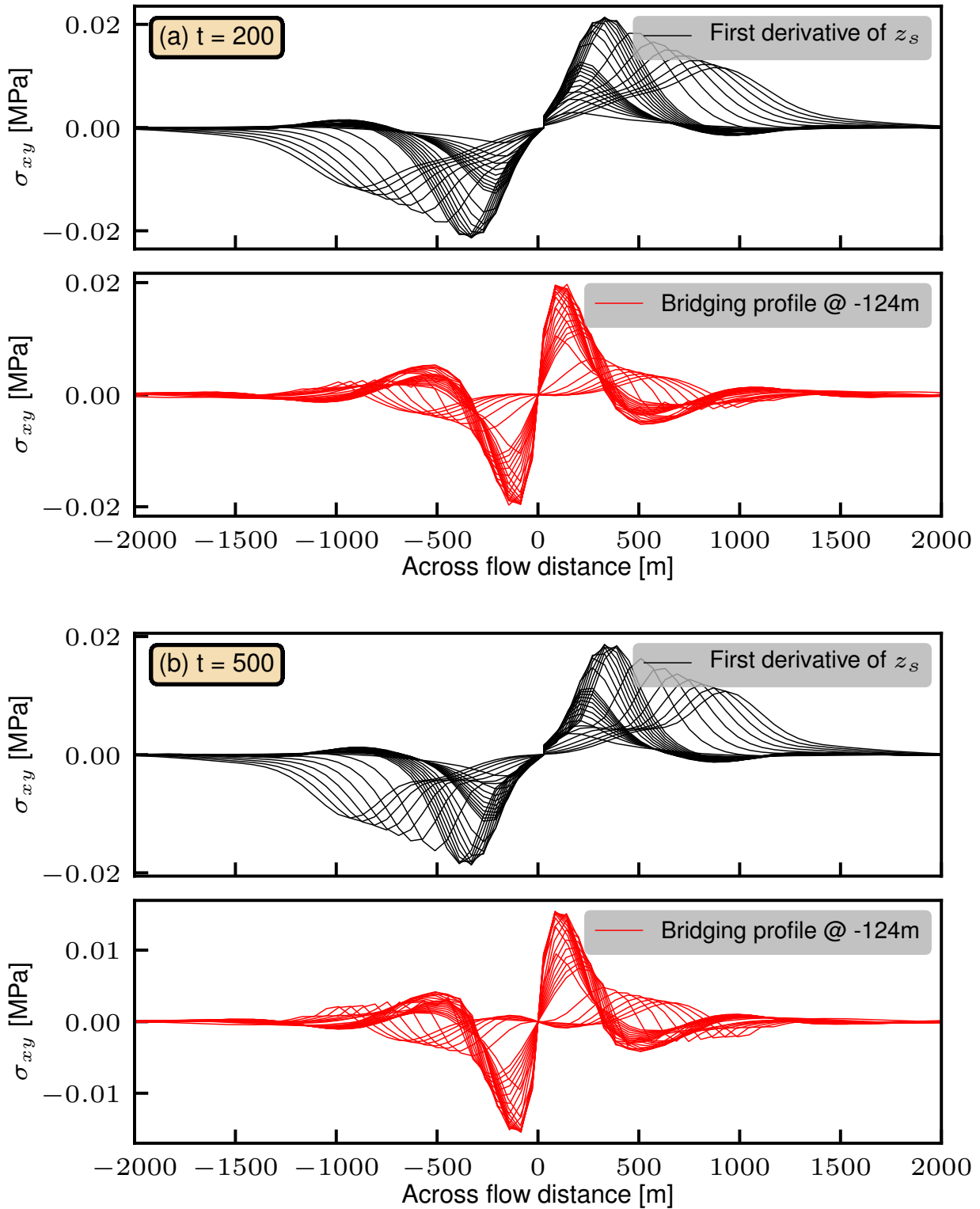


**Figure 19.: (a)** shows first derivative of top surface  $z_s$  for all model-runs after 200 years (top, black) and bridging profile at -124 m for all model-runs (bottom, red) after 200 years. **(b)** shows first derivative of top surface  $z_s$  for all model-runs after 200 years (top, black) and bridging profile at -124 m for all model-runs (bottom, red) after 500 years.